Shear banding, intermittency, jamming, and dynamic phases for skyrmions in inhomogeneous pinning arrays

C. Reichhardt and C. J. O. Reichhardt

Theoretical Division and Center for Nonlinear Studies, Los Alamos National Laboratory, Los Alamos, New Mexico 87545, USA

We examine driven skyrmion dynamics in systems with inhomogeneous pinning where a strip of strong pinning coexists with a region containing no pinning. For driving parallel to the strip, we find that the initial skyrmion motion is confined to the unpinned region and the skyrmion Hall angle is zero. At larger drives, a transition occurs to a phase in which motion also appears within the pinned region, creating a shear band in the skyrmion velocity, while the skyrmion Hall angle is still zero. As the drive increases further, the flow becomes disordered and the skyrmion Hall angle increases with drive until saturating at the highest drives when the system transitions into a moving crystal phase. The different dynamic phases are associated with velocity and density gradients across the pinning boundaries. We map out the dynamic phases as a function of pinning strength, skyrmion density, and Magnus force strength, and correlate the phase boundaries with features in the velocity-force curves and changes in the local and global ordering of the skyrmion structure. For large Magnus forces, the shear banding instability is replaced by large-scale intermittent flow in the pinned region accompanied by simultaneous motion perpendicular to the direction of the drive, which appears as oscillations in the transport curves. We also examine the case of a drive applied perpendicular to the strip, where we find a jamming effect in which the skyrmion flow is blocked by skyrmion-skyrmion interactions until the drive is large enough to induce plastic flow.

I. INTRODUCTION

Skyrmions in magnetic systems were discovered in MnSi in 2009 [1], and since that time skyrmions have been found in an increasing variety of systems, including materials in which the skyrmions are stable at room temperature [2–6]. In samples with weak quenched disorder, the skyrmions form a triangular lattice and can be set into motion with an applied current [7–11]. When disorder is present, there is a finite depinning threshold for skyrmion motion and there can be different types of flow such as plastic or ordered as well as transitions between different types of moving phases [3,4,6,7,9,11–16]. The onset of motion and the dynamic phase transitions are correlated with changes in the skyrmion velocity-force curves, the skyrmion flow patterns, the structure factor, and the velocity noise spectra [17].

Although skyrmions have many similarities to other systems that are known to exhibit depinning, such as vortices in type-II superconductors or colloidal particles on rough landscapes [18], they also have the unique feature of a strong nondissipative Magnus force which creates velocity components that are perpendicular to the forces produced by the drive, pinning, and interaction with other skyrmions. The ratio of the Magnus force to the dissipation can range from a few percent to up to a factor of 10 or more [3,9,19]. One consequence of the Magnus force is that under a drive, skyrmions display a strong gyroscopic motion that produces a finite Hall angle known as the skyrmion Hall angle [3,13–15,20–22]. The gyroscopic motion generates spiraling skyrmion orbits in

confining potentials or pinning sites [23–25] which have been proposed to be one reason why the pinning of skyrmions is often weak, since a skyrmion can spiral around pinning sites rather than becoming trapped [3,7,9]. There are, however, other cases in which the effect of pinning on skyrmions can be strong [4,14,15].

The skyrmion Hall angle is constant in the absence of pinning or disorder, but in the presence of disorder it develops a dependence on drive or velocity, starting at a value of zero just at the depinning threshold and gradually increasing with increasing skyrmion velocity until saturating at high drives to a value close to that found in the clean limit [13–15,26–31]. Particle-based [13,24,26,32,33] and continuum-based [15,24,27,30] simulations show that the drive dependence of the skyrmion Hall angle is a result of the skyrmion-pin interactions. In regimes of collective skyrmion motion in the presence of quenched disorder, the flow above depinning can be elastic when the pinning is weak, with all skyrmions maintaining the same neighbors as they move [8,9,13,32], or it can be plastic [13,15,26,34,35], with a combination of pinned and moving skyrmions. In some cases, the skyrmions exhibit intermittent or avalanche-like flow, in which sudden bursts of motion are interspersed among intervals in which no motion occurs [36,37].

In systems that exhibit depinning, such as superconducting vortices [38,39], colloidal assemblies [40,41], electron crystals [42,43], or charge density waves [44], the disorder is often homogeneous on long length scales, so that on average, the same depinning threshold occurs throughout the sample and

054423-1

there is a single well-defined depinning drive. It is also possible for samples to contain strongly inhomogeneous pinning, where strong pinning in some portions of the sample coexists with other regions in which the pinning is absent or weak. This type of pinning can arise naturally if the system has large-scale inhomogeneities, or it can be created artificially using lithographic techniques by writing a pinning array into only selected portions of the sample while other portions of the sample remain pin-free. In colloidal systems with inhomogeneous pinning, it was shown that flow occurs in the unpinned regions and that shear banding effects arise when a portion of the colloids in the unpinned region are either pinned or moving more slowly due to interactions with neighboring pinned colloids, creating a velocity gradient [45,46]. Other studies of colloidal systems containing a strip of pinned colloids revealed that the system effectively freezes from the pinned strip outward into the bulk [47]. In superconducting systems, coexisting regions of strong pinning and weak pinning were created by patterned irradiation in order to study shearing effects in the vortex lattice when flow initiates in the unpinned regions and strong velocity gradients appear [48–52]. It is also possible to create spatially inhomogeneous pinning by creating large-scale thickness modulations [53–56], diluting periodic pinning arrays [57,58], or by selecting a sample with strong edge pinning but weak bulk pinning [59]. Another way to introduce inhomogeneous depinning thresholds is by creating a gradient in the number or size of the pinning sites; in this case, the dynamics depend on whether the system is driven parallel or perpendicular to the gradient [60–64]. Other studies showed that inhomogeneous pinning can lead to a number of interesting dynamical effects such as negative mobility [65] and ratchet motion [66,67]. In charge density wave systems with inhomogeneous pinning, depinning first occurs in the weak pinning region, creating a shearing effect in the more strongly pinned region [68]. In systems with spatially inhomogeneous pinning, application of a drive tends to create velocity gradients which lead to the formation of dislocations, the emergence of liquid phases, or the coexistence of liquid and solid phases. Many of these phases are similar to those found in systems with homogeneous pinning or no pinning when the driving is inhomogeneous, such as in Corbino geometries for superconducting vortices, where different phases appear such as a solid flow in which the vortex lattice rotates as a rigid body, as well as a shear banded state at higher drives [69–75].

In the studies performed with inhomogeneous pinning up until now, the dynamics has been exclusively overdamped, so it is not known what happens when there is a finite Magnus force. Since the Magnus force mixes the velocity components from external drives, one would expect rather different results to appear compared to what is found in the overdamped systems. Another interesting effect is that shear banding could arise for driving either parallel or perpendicular to the inhomogeneous pinning regions due to the Magnus force. There have been some studies of skyrmions under inhomogeneous drives in the absence of pinning which produced evidence for rigid flow, disordered flow, and shear banding effects [76–78].

Here we examine skyrmion dynamics in a system where the external drive is uniform but the pinning is inhomogeneous, with a region of strong pinning in the form of a strip

coexisting with a region where there is no pinning. When the drive is parallel to the strip, we find that the skyrmions first move in the unpinned region and that the skyrmion Hall effect is suppressed. As the drive is increased, flow occurs in both regions with a velocity gradient in the pinned region, but the skyrmion Hall angle is still zero. At higher drives, a shear-induced disordered or liquid phase appears due to a proliferation of topological defects in the skyrmion lattice, and the skyrmion Hall angle becomes finite, while at very high drives, the flow becomes uniform, the skyrmions form a moving liquid or moving crystal state, and the skyrmion Hall angle reaches a saturation value. For a drive applied perpendicular to the strip, when the Magnus force is large we find that skyrmions from the unpinned region enter the pinned region in avalanches, creating a density gradient analogous to the Bean state found in type-II superconductors [79,80]. Here the skyrmions accumulate along the edge of the pinned region and form a jammed state in which the repulsive interactions from the skyrmions in the pinned region block the flow of the skyrmions in the unpinned region. In previous work on skyrmion motion in inhomogeneous pinning, we considered only the case of skyrmion flow in the unpinned region [81]. Here we expand on this to study the entire range of dynamics and the interplay of motion in both the unpinned and pinned regions as well as driving in different directions. Although we focus on skyrmions, our results should be applicable to other types of systems with a Magnus force or gyroscopic coupling in the presence of inhomogeneous disorder. Examples of such systems include colloidal rotators [82], magnetically driven colloids [83–85], vortices in superfluids [86,87], and chiral active matter states [88–90].

II. SIMULATION

We consider a two-dimensional system of size $L \times L$ with periodic boundary conditions in the x and y directions where the skyrmions are modeled as particles with skyrmion-skyrmion and skyrmion-pinning interactions based on a modified Thiele equation [13,26,91–93]. Half of the sample is pin-free, and the other half of the sample contains a square array of pinning sites, as illustrated in Fig. 1. The pinning sites are modeled as finite range parabolic traps with lattice constant a, pinning radius r_p, and maximum strength F_p. The sample contains N_p pinning sites and N skyrmions, and we focus on the case of $N/N_p = 2.0$, so that under equilibrium conditions the skyrmion density is uniform, with half of the skyrmions in the pinned region and half of the skyrmions in the unpinned region. We define the matching density $n_\phi = 2N_p/L^2$ to be the density at which the number of skyrmions would match the number of pinning sites if the entire sample were filled with the same density of pinning as the pinned region. Throughout this work we consider $n_\phi = 0.4$.

The dynamics of skyrmion i is governed by the following equation of motion:

$$\alpha_d \mathbf{v}_i + \alpha_m \hat{z} \times \mathbf{v}_i = \mathbf{F}_i^{ss} + \mathbf{F}_i^D. \quad (1)$$

Here the repulsive skyrmion-skyrmion force is $\mathbf{F}_i = \sum_{j=1}^{N} K_1(r_{ij})\hat{\mathbf{r}}_{ij}$, where $r_{ij} = |\mathbf{r}_i - \mathbf{r}_j|$, $\hat{\mathbf{r}}_{ij} = (\mathbf{r}_i - \mathbf{r}_j)/r_{ij}$, and the modified Bessel function $K_1(r)$ falls off exponentially for large r. A uniform driving force $\mathbf{F}^D = F_D \hat{\alpha}$ is applied to
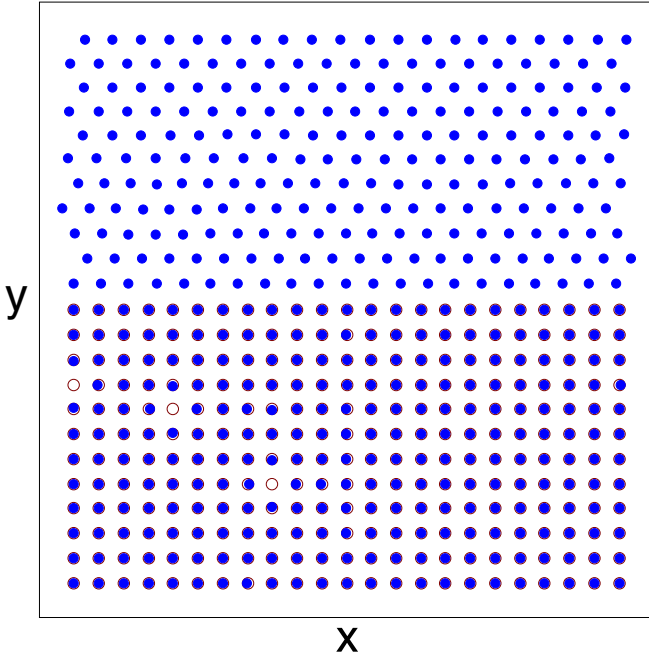
FIG. 1. Image of the system showing skyrmion positions (blue dots) and pinning site locations (open red circles). There are half as many skyrmions as pinning sites and only the lower half of the sample contains pinning. The drive can be applied along either the x or the y direction.

all skyrmions in either the x direction ($\alpha = x$), parallel to the pinning strip, or in the y direction ($\alpha = y$), perpendicular to the pinning strip. The skyrmion velocity is $\mathbf{v}$, and the damping term α_d aligns the velocity in the direction of the net applied forces. The Magnus term, with coefficient α_m, creates velocities that are perpendicular to the net external forces. When the Magnus term is finite, in the absence of pinning the skyrmions move at an angle with respect to the driving force given by the intrinsic skyrmion Hall angle $\theta_{sk}^{int} = \tan^{-1}(\alpha_m/\alpha_d)$.

The initial skyrmion positions are obtained through simulated annealing, after which we apply a drive which we increase in increments of δF_D with a fixed number of simulation time steps spent at each value of F_D. For each value of the drive, we measure the average velocity both parallel, $\langle V_{||} \rangle = N^{-1} \sum_i^N \mathbf{v}_i \cdot \hat{\mathbf{x}}$, and perpendicular, $\langle V_{\perp} \rangle = N^{-1} \sum_i^N \mathbf{v}_i \cdot \hat{\mathbf{y}}$, to the pinning strip. The measured skyrmion Hall angle is $\theta_{sk} = \tan^{-1}(\langle V_{\perp} \rangle / \langle V_{||} \rangle)$. For the studies reported here we typically use increments of $\delta F_D = 0.00025$ and we wait 2000 simulation time steps between force increments. The velocity-force characteristics and average measured quantities do not change for smaller force increments or longer waiting times.

III. SHEARING DYNAMICS FOR PARALLEL DRIVING

We first consider the case where the skyrmions are driven in the x direction, parallel to the pinning stripe. In Fig. 2(a) we plot $\langle V_{||} \rangle$ and $\langle V_{\perp} \rangle$ versus F_D for a sample with $F_p = 0.75$ and $\alpha_m/\alpha_d = 1.0$. In the absence of pinning, the skyrmions form a triangular lattice that moves at an angle of $45°$ with respect to the x axis, as indicated by the dashed blue line.
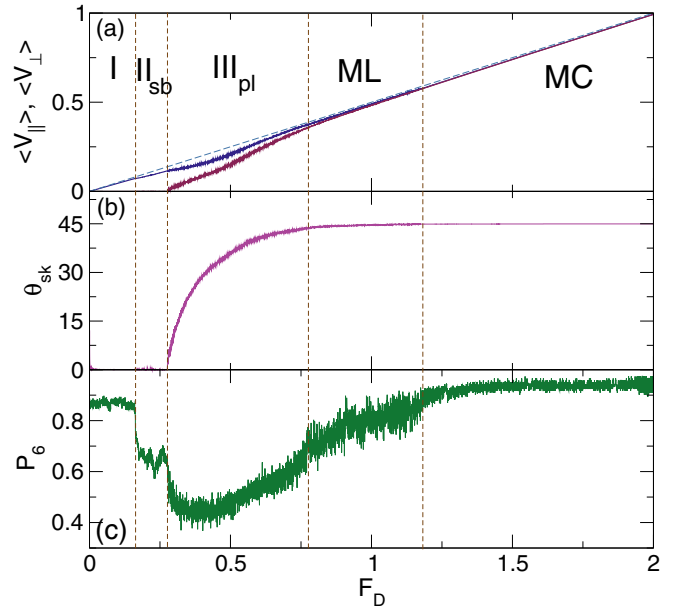

FIG. 2. (a) $\langle V_{||} \rangle$ (blue solid line) and $\langle V_{\perp} \rangle$ (red line) vs F_D for a sample with x direction driving at $F_p = 0.75$ and $\alpha_m/\alpha_d = 1.0$. Vertical dashed lines indicate the four dynamical phases: I, longitudinal flow in the x direction in only the pin-free channel; II$_{sb}$, the shear banding phase; III$_{pl}$, plastic flow; ML, a moving liquid; and MC, a moving crystal. (b) The corresponding skyrmion Hall angle θ_{sk} vs F_D showing that θ_{sk} increases from zero in phase III$_{pl}$ and reaches a saturation value in the ML and MC phases. (c) The corresponding fraction of sixfold coordinated skyrmions P_6 vs F_D, showing changes across each of the four dynamic phase transitions.

Figure 2(b) shows the corresponding measured skyrmion Hall angle θ_{sk} versus F_D. As indicated in Fig. 2(a), we identify five dynamic phases. In phase I, $\langle V_{||} \rangle$ is finite and $\langle V_{\perp} \rangle = 0.0$, and the skyrmions flow only in the unpinned portions of the sample in the direction of the drive. This motion is illustrated in Fig. 3(a), where the skyrmions flow elastically inside the pin-free region and the skyrmion Hall angle is zero. As the drive increases, the system enters the shear banding phase II$_{sb}$ where the flow is still only along the x direction but skyrmions move both in the unpinned region and in the pinned region, as shown in Fig. 3(b). In phase II$_{sb}$, the skyrmions in the unpinned region begin to accumulate along one edge of the pinned region due to the Magnus force, which acts along the y direction perpendicular to the pin-free region. For $F_D > 0.28$, in phase III$_{pl}$ or the plastic flow state there is now flow in both the x and y directions and skyrmions can move across the entire pinned strip. Within the pinned region there is a combination of pinned and moving skyrmions which creates the disordered motion illustrated in Fig. 3(c). The skyrmion Hall angle θ_{sk} increases from zero in phase III$_{pl}$ and it begins to saturate once $F_D/F_p \gtrsim 1.0$. When $0.75 < F_D < 1.18$, all the skyrmions are moving since $F_D > F_p$; however, the flow is still disordered, and the system is in the moving liquid phase ML. For $F_D > 1.18$, there is a transition to a moving crystal (MC) phase of the type shown in Fig. 3(d). Within the ML phase, the increase of θ_{sk} with increasing F_D is less rapid compared to phase III$_{pl}$, while within the MC phase, θ_{sk} is constant at the clean limit value of $\theta_{sk} \approx 45°$, and fluctuations
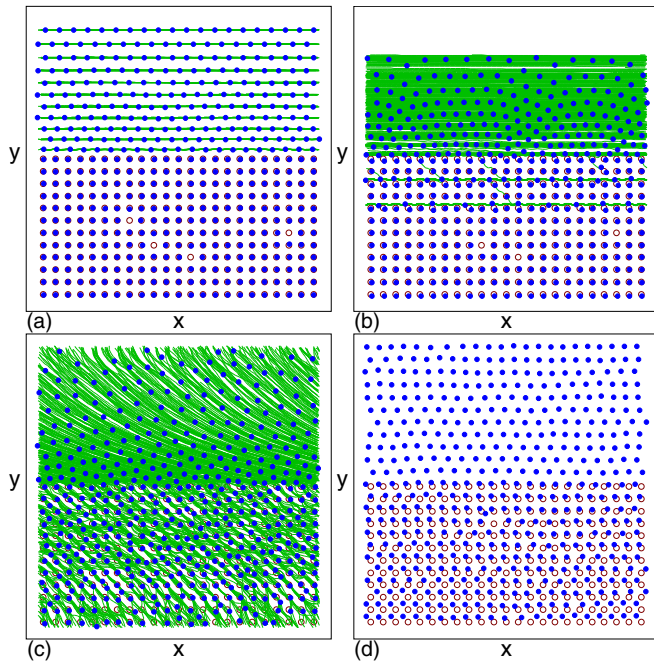
FIG. 3. Skyrmion locations (blue dots), pinning site locations (open circles), and skyrmion trajectories (green lines) during a fixed time interval for the system in Fig. 2 with x direction driving at $F_p = 0.75$ and $\alpha_m/\alpha_d = 1.0$. (a) Phase I at $F_D = 0.1$, where the flow is only in the unpinned region. (b) Phase II$_{sb}$ at $F_D = 0.2$, where there is flow in both the unpinned and pinned regions but the skyrmion Hall angle is zero. (c) Phase III$_{pl}$ at $F_D = 0.5$ where the skyrmion Hall angle is finite. (d) The pinning sites and skyrmion locations without trajectories in the moving crystal phase MC at $F_D = 1.5$.

in $\langle V_{||} \rangle$ and $\langle V_\perp \rangle$ are strongly reduced. The vertical lines in Fig. 2 indicate the transitions between the five different phases. To better highlight the I-II$_{sb}$ transition, in Fig. 4 we show a blowup of $\langle V_{||} \rangle$ and $\langle V_\perp \rangle$ versus F_D, where the blue dashed line indicates the expected value of $\langle V_{||} \rangle$ in a pin-free system. Across the I-II$_{sb}$ transition, there is a change
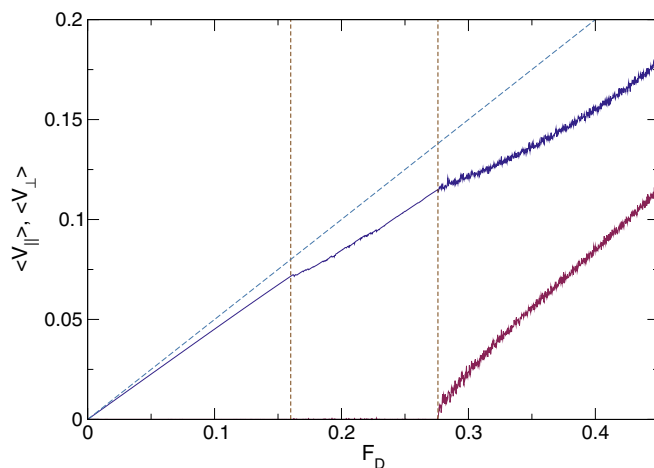

FIG. 4. A blowup of the $\langle V_{||} \rangle$ (blue solid line) and $\langle V_\perp \rangle$ (red line) vs F_D curves from Fig. 2(a) highlighting the I-II$_{sb}$ transition at $F_D = 0.16$. The blue dashed line is the velocity $\langle V_{||} \rangle$ in the pin-free limit.

in the slope of $\langle V_{||} \rangle$ as a function of F_D when skyrmions in the pin-free region start to accumulate along the edge of the pinned region and the skyrmions in the pinned region begin to move in the x direction.

Another method for characterizing the different phases is to measure the fraction P_6 of sixfold coordinated skyrmions. We generate a Voronoi construction from the skyrmion positions to identify the coordination number z_i of each skyrmion, and then obtain $P_6 = N^{-1} \sum_i^N \delta(6 - z_i)$. In Fig. 2(c), P_6 versus F_D has a signature at all four phase transitions. In phase I, the ordering is mostly triangular due to the arrangement of the skyrmions in the pin-free region, as shown in Fig. 1, and P_6 also picks up some finite weight in the pinned region due to small distortions that can produce short additional sides in the Voronoi polygons. When the system enters the II$_{sb}$ phase, there is a drop in P_6 due to the formation of dislocations that glide along the x direction. There is another sharp drop in P_6 at the onset of the strongly disordered III$_{pl}$, where topological defects proliferate. In the ML phase, there is more topological order and P_6 increases to $P_6 \approx 0.825$, but a number of dislocations are still present in the sample. Upon entering the MC phase, $P_6 \approx 0.95$ since the skyrmions exhibit crystalline order.

The dynamic phases are also associated with changes in the structure factor $S(\mathbf{q})$. In Fig. 5(a) we plot $S(\mathbf{q})$ for the system from Fig. 2 in phase I at $F_D = 0.1$, where we find a combination of both square and triangular peaks which reflects the square ordering of the skyrmions in the pinned portion of the sample and the triangular ordering of the skyrmions in the unpinned region. In phase II$_{sb}$ at $F_D = 0.2$ in Fig. 5(b), the ordering is more smectic with enhanced peaks along certain directions due to the sliding of the skyrmions along the pinning rows. For $F_D = 0.5$ in phase III$_{pl}$, Fig. 5(c) shows that a square ordering has emerged due to the pinned skyrmions, along with a smooth background produced by the liquid structure of the other skyrmions. In Fig. 5(d) at $F_D = 1.0$ in the ML phase, a ring structure appears along with sixfold peaks, indicating that there is some short-range translational order imposed on the liquid structure. In the MC phase at $F_D = 1.5$ in Fig. 5(e), the vortices have triangular ordering and there are six clear peaks. When the pinning strength is raised to $F_p = 1.0$ in the same system, Fig. 5(f) indicates that there is a moving square lattice, which we discuss in Sec. IV.

The spatial distribution of the velocities has distinct structures in the different phases. In Figs. 6(a) and 6(b) we plot $\langle V_{||} \rangle$ and $\langle V_\perp \rangle$ averaged over the x direction as a function of y in phase I at $F_D = 0.04$ for the system in Fig. 2. The vertical dashed line indicates the edge of the pinned region at $y = 18$. We find $\langle V_{||} \rangle \approx 0.04$ in the unpinned region and $\langle V_{||} \rangle = 0$ in the pinned region, while $\langle V_\perp \rangle$ is zero in both the pinned and unpinned regions. As F_D increases, the skyrmion density in the unpinned region at the largest values of y decreases since the skyrmion lattice is being compressed along the y direction. In Figs. 6(c) and 6(d) we show the x direction average values of $\langle V_{||} \rangle$ and $\langle V_\perp \rangle$ versus y in phase II$_{sb}$ at $F_D = 0.25$, where the parallel velocity is finite in the pinned region and the skyrmion density is close to zero for $y > 35$. There are several peaks in V_x in the pinned region that decrease in height as y decreases, indicating that the motion in the pinned region is
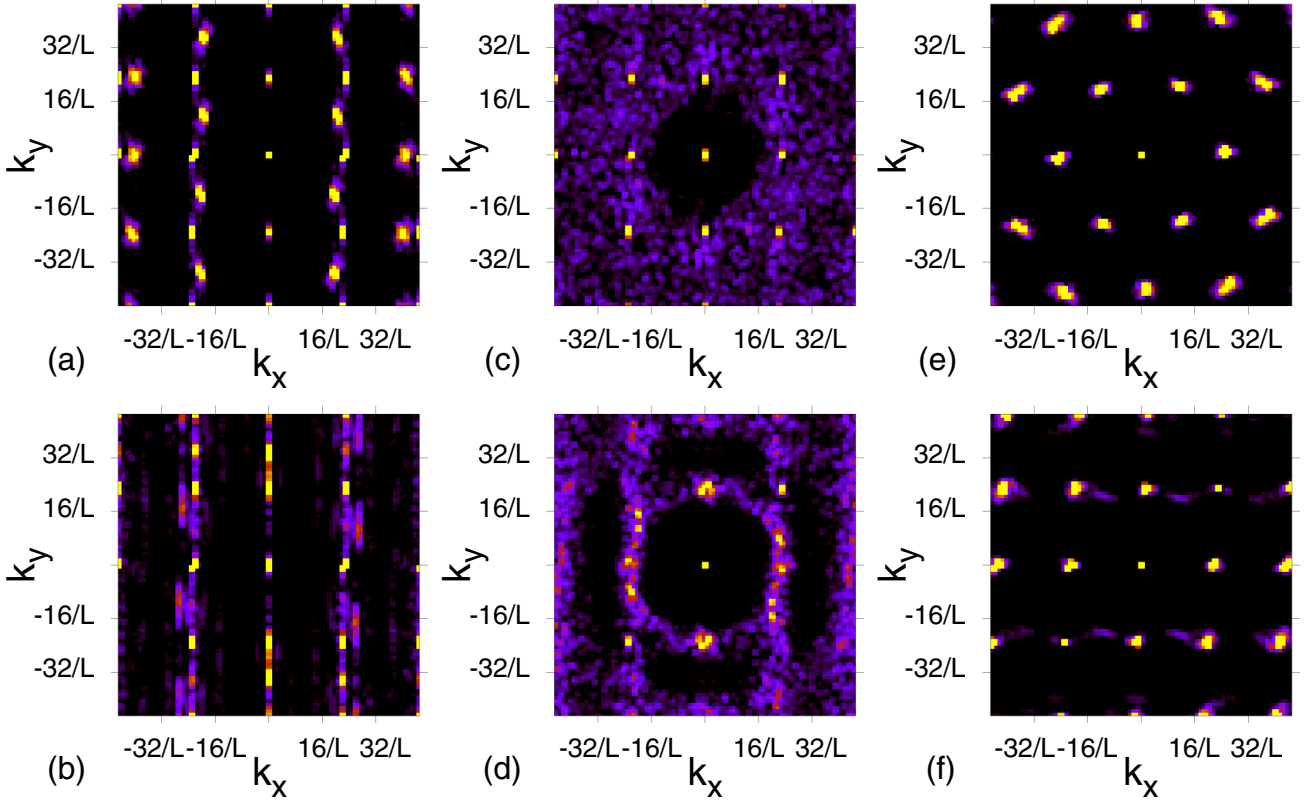
FIG. 5. The structure factor $S(\mathbf{q})$ for the system in Fig. 2 with x direction driving at $F_p = 0.75$ and $\alpha_m/\alpha_d = 1.0$. (a) Phase I; (b) Phase II$_{sb}$; (c) Phase III$_{pl}$; (d) ML phase; (e) MC phase. (f) The same system at $F_p = 1.0$ has a moving square lattice phase described in Sec. IV.

largest close to the edge of the pinning that is exposed to the largest density of moving skyrmions in the pin-free channel. Throughout phase II$_{sb}$, $\langle V_\perp \rangle = 0$.

In Figs. 7(a) and 7(b) we plot the x direction average values of $\langle V_\parallel \rangle$ and $\langle V_\perp \rangle$ versus y in phase III$_{pl}$ at $F_D = 0.5$. The

velocity is finite both parallel and perpendicular to the drive, and the values of both $\langle V_\parallel \rangle$ and $\langle V_\perp \rangle$ are lowest in the pinned region. A peak in $\langle V_\parallel \rangle$ appears in the unpinned region near the edge of the pinning due to a combination of an increase in the skyrmion density with a speed-up or acceleration effect in
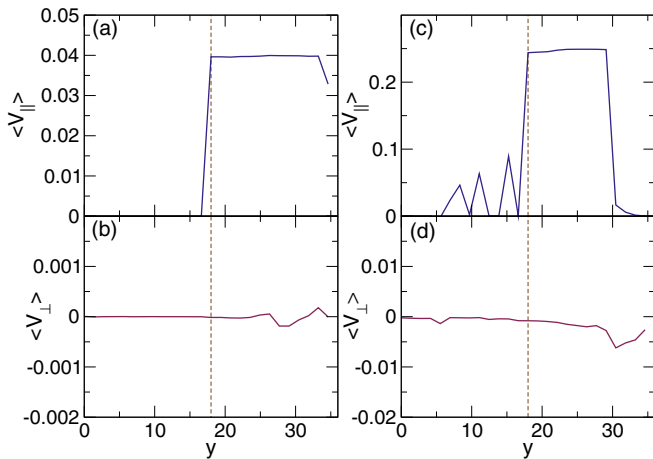

FIG. 6. The velocities spatially averaged over the x direction as a function of y for the system in Fig. 2 with x direction driving at $F_p = 0.75$ and $\alpha_m/\alpha_d = 1.0$. (a) $\langle V_\parallel \rangle$ and (b) $\langle V_\perp \rangle$ in phase I at $F_D = 0.04$. (c) $\langle V_\parallel \rangle$ and (d) $\langle V_\perp \rangle$ in phase II$_{sb}$ at $F_D = 0.25$. The vertical dashed lines indicate the separation between the pinned region ($y \leqslant 18$) and the pin-free region ($y > 18$).
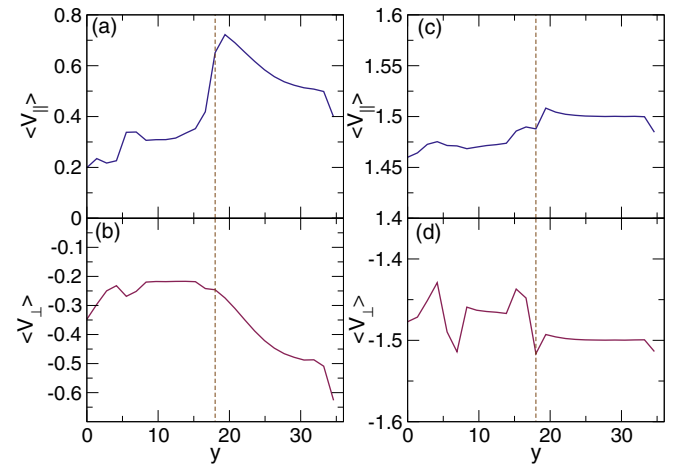
FIG. 7. The velocities spatially averaged over the x direction as a function of y for the system in Fig. 2 with x direction driving at $F_p = 0.75$ and $\alpha_m/\alpha_d = 1.0$. (a) $\langle V_\parallel \rangle$ and (b) $\langle V_\perp \rangle$ in phase III$_{pl}$ at $F_D = 0.5$. (c) $\langle V_\parallel \rangle$ and (d) $\langle V_\perp \rangle$ in the MC phase at $F_D = 1.5$. The vertical dashed lines indicate the separation between the pinned region ($y \leqslant 18$) and the pin-free region ($y > 18$).
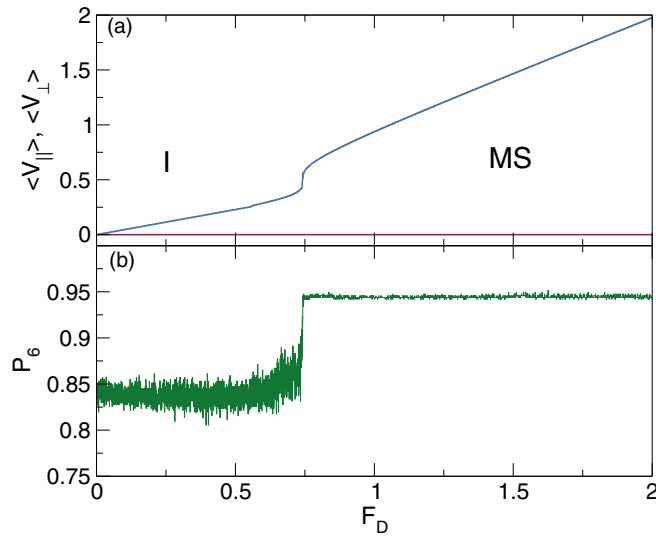
FIG. 8. (a) $\langle V_{||} \rangle$ (blue) and $\langle V_{\perp} \rangle$ (red) vs F_D for the system in Fig. 2 with x direction driving at $F_p = 0.75$ and $\alpha_m/\alpha_d = 0$. We find phase I and a moving smectic (MS) phase as illustrated in Fig. 9. (b) The corresponding fraction of sixfold coordinated skyrmions P_6 vs F_D showing that in the MS phase there is a jump up to $P_6 = 0.95$.

which the skyrmions in the pinned region exert a force on the unpinned skyrmions that is perpendicular to the drive. This force is rotated into the driving direction by the Magnus term, contributing an extra velocity component to the skyrmions in the unpinned region. A similar acceleration or speed-up effect was observed for skyrmions interacting with planar defects in the form of periodic quasi-one-dimensional potentials [94]. Figures 6(c) and 6(d) shows the x-averaged values of $\langle V_{||} \rangle$ and $\langle V_{\perp} \rangle$ versus y in the MC phase at $F_D = 1.5$. Here the velocities in both directions are nearly independent of y since the effect of the pinning is greatly reduced.

A. Dynamic phases at small Magnus forces

We next consider the effect of varying the relative strength of the Magnus force. We observe three regimes of behavior consisting of the low Magnus force regime for $0 \leqslant \alpha_m/\alpha_d \leqslant 0.5$, the intermediate Magnus force regime for $0.5 < \alpha_m/\alpha_d < 7.0$, and the high Magnus force regime for $\alpha_m/\alpha_m \geqslant 7.0$. Each regime has distinctive dynamics.

The low Magnus force regime is relevant not only for skyrmion systems but also for certain superconducting vortex systems [95]. In Fig. 8(a) we plot $\langle V_{||} \rangle$ and $\langle V_{\perp} \rangle$ versus F_D for the system in Fig. 2 with $F_p = 0.75$ and $\alpha_m/\alpha_m = 0$. We find two dynamic phases. In phase I, flow occurs only in the unpinned region, while at higher drives we observe a moving smectic (MS) phase in which all of the skyrmions are flowing in both the pinned and unpinned regions. In both phases, $\langle V_{\perp} \rangle = 0$. We note that there can be some shear banding flows near the I-MS transition, which produce the nonlinear behavior in $\langle V_{||} \rangle$ near $F_D/F_p = 1.0$. This phenomenon has been discussed previously in more detail for the overdamped regime [64]. Figure 8(b) shows the corresponding P_6 versus F_D where we observe a jump from $P_6 = 0.85$ in phase I to $P_6 = 0.95$ in the MS phase. The value of P_6 is less than 1.0 due
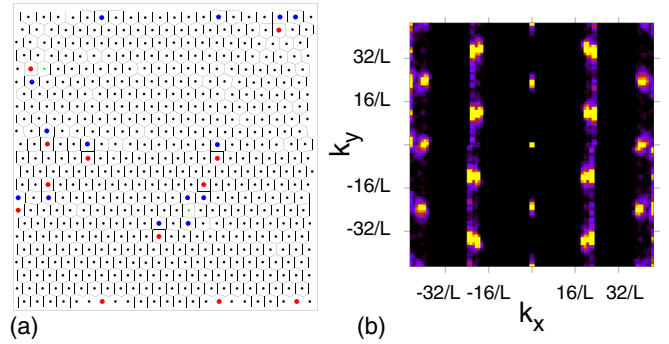

FIG. 9. The Voronoi construction for the skyrmion locations for the system in Fig. 8 with x direction driving at $F_p = 0.75$ and $\alpha_m/\alpha_d = 0$ at $F_D = 1.0$ in the MS phase. The coordination number of individual skyrmions is 5 (red), 6 (black), 7 (blue), or outside the range of 5–7 (green). Fivefold and sevenfold coordinated defects form pairs that have their Burgers vector aligned with the driving direction. (b) The corresponding structure factor $S(\mathbf{k})$ indicates the presence of smectic order.

to pinning-induced dislocations in the skyrmion lattice. These dislocations cause the skyrmions in the pinned portion of the sample to move a bit more slowly than the skyrmions in the unpinned region, producing a net slip between the two spatial regions. In Fig. 9(a) we plot the Voronoi construction for the instantaneous skyrmion positions in the MS phase at $F_D = 1.0$. Here, fivefold and sevenfold coordinated defects form pairs with their Burgers vector parallel to the driving direction. Transient states produced either by the motion of a 5-7 defect pair by one lattice constant or by the temporary overlap of two oppositely oriented 5-7 defect pairs are responsible for the appearance in Fig. 9(a) of skyrmions that have less than five or more than seven neighbors. In the corresponding $S(\mathbf{k})$, shown in Fig. 9(b), there is strong smectic ordering, but six peaks are still present due to the partial triangular ordering of the moving lattice.

For finite but small α_m/α_d, we still find phase I and the MS phase; however, at higher drives, an additional transition occurs when the skyrmion lattice decouples from the pinning, ceases to be locked in the driving direction, and exhibits a finite skyrmion Hall angle. In Figs. 10(a)–10(c) we plot $\langle V_{||} \rangle$, $\langle V_{\perp} \rangle$, and P_6, respectively, versus F_D for the same system in Fig. 8 but at $\alpha_m/\alpha_d = 0.0125$, where the skyrmions have an intrinsic Hall angle of $\theta_{sk}^{int} = 0.7125°$. The vertical lines distinguish the different dynamical phases. We find extended regions of phase I and the MS phase, in which $\langle V_{\perp} \rangle = 0$. For $5.9 < F_D < 8.5$, the system becomes disordered, as indicated by the drop in P_6 to $P_6 \approx 0.75$, and the system forms a moving liquid. Here $\langle V_{\perp} \rangle$ becomes finite as the system begins to show a finite skyrmion Hall angle. For $F_D > 8.5$, P_6 jumps up to $P_6 = 0.985$ when the system enters a moving crystal phase. In the MC phase the topological ordering is higher than in the MS since the skyrmion lattice is no longer locked to the square pinning array. The MS-MC transition is accompanied by a change in the slope of $\langle V_{\perp} \rangle$.

In Fig. 11(a) we show the skyrmion locations, pinning site locations, and skyrmion trajectories in the MS phase for the system in Fig. 10 at $F_D = 2.5$. The image in Fig. 11(b)
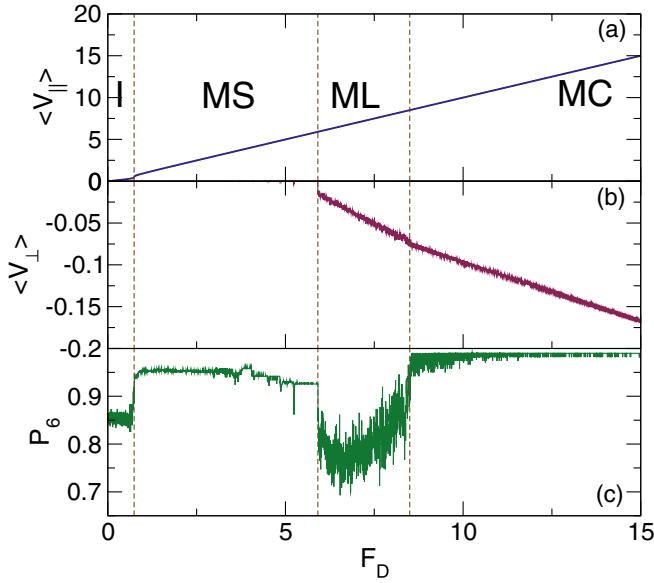
FIG. 10. (a) $\langle V_\parallel \rangle$, (b) $\langle V_\perp \rangle$, and (c) P_6 vs F_D for the sample in Fig. 2 with x direction driving at $F_p = 0.75$ and $\alpha_m/\alpha_d = 0.0125$. The vertical lines distinguish the different dynamic phases. I, longitudinal flow in only the pin-free channel; MS, moving smectic; ML, moving liquid; MC, moving crystal. A drop in P_6 marks the window of disordered moving liquid between the moving smectic (MS) and moving crystal (MC) phases.

FIG. 11. Skyrmion locations (blue dots) and pinning site locations (open circles) for the system in Fig. 10 with x direction driving at $F_p = 0.75$ and $\alpha_m/\alpha_d = 0.0125$. (a) The MS phase at $F_D = 2.5$, with skyrmion trajectories during a fixed time interval drawn as green lines. (b) The same as (a) with only the skyrmion locations shown, indicating that the skyrmion lattice is aligned in the x direction, parallel to the drive. (c) The ML phase at $F_D = 7.0$. (d) The MC phase at $F_D = 7.5$.

of only the skyrmion locations in the same state indicates that the skyrmion lattice is aligned with the x axis, parallel to the driving direction. As F_D increases in the MS phase, the skyrmions in the pin-free region become compressed and row reductions occur, producing the drops in P_6 in the MS phase at $3.0 < F_D < 5.9$ in Fig. 10(c). At $F_D = 7.0$ in the ML phase, illustrated in Fig. 11(c), the skyrmions in the pinned region tend to remain aligned with the x axis while the rest of the skyrmions have adopted a rotated configuration. The formation of a strongly driven moving liquid state occurs due to the competition between the pinning, which tends to lock the skyrmion motion along the x axis, and the Magnus force, which favors skyrmion motion at an angle of 7° with respect to the x axis. At the MS-ML transition, the dislocations that were gliding in the MS phase generate a temporary proliferation of additional topological defects that dynamically anneal away as F_D increases and the skyrmions enter the MC phase, illustrated in Fig. 11(d) at $F_D = 7.5$.

In general, increasing the drive reduces the dynamical effect of the pinning, as found in other systems that exhibit depinning [18], and eventually the effective pinning strength becomes weak enough that the skyrmions can start jumping in the direction transverse to the drive. The guiding of particles along a symmetry direction of a periodic pinning array has been well studied in overdamped systems, where the particles tend to lock to symmetry directions of the pinning lattice even when these directions are not aligned with the direction of the external drive [18,96,97]. This effect has also been studied for individual skyrmions moving in periodic pinning arrays using both a particle-based model [98] and continuum-based simulations [99]. For skyrmion assemblies, the locking effect
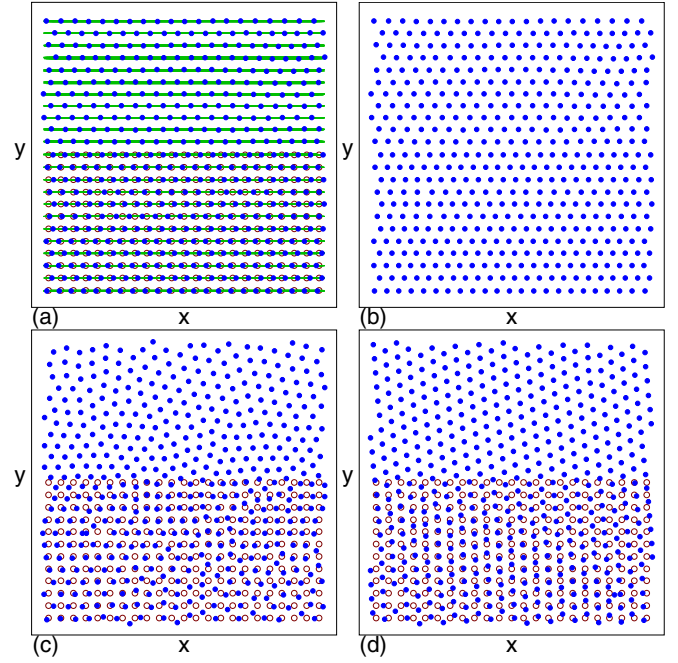
is generally weaker, but it can be observed for driving over square pinning arrays along 0° and 45° from the major symmetry axis of the lattice. The MS-ML and ML-MC transitions shift to higher values of F_D with decreasing α_m/α_d, and at $\alpha_m/\alpha_d = 0$, the system remains locked in the MS phase for all drives above depinning.

In Fig. 12(a) we plot $\langle V_\parallel \rangle$ and $-\langle V_\perp \rangle$ versus F_D for the same system in Fig. 10 at a higher value of $\alpha_m/\alpha_d = 0.25$, which corresponds to $\theta_{sk}^{int} = 14°$. The corresponding P_6 versus F_D in Fig. 12(b) shows a transition from phase I to the plastic flow phase III$_{pl}$ followed by a transition directly into the moving crystal phase, with no MS phase.

We construct a dynamic phase regime as a function of F_D versus α_m/α_d in Fig. 13(a) for the low Magnus force systems in Figs. 10–12. The MS phase only occurs when $\alpha_m/\alpha_d < 0.1$. In Fig. 13(b) we replot the phase diagram on a log-log scale. The dashed line is a fit to $F_D \propto 1/(\alpha_m/\alpha_d)$ indicating that the drives at which the MS-ML and ML-MC transitions occur diverge as the relative strength of the Magnus force decreases. An interesting aspect of this result is that it suggests that in a system such as superconducting vortices with a small but finite Magnus force, there could be a transition from a moving smectic to a moving crystal state at a finite but large drive.

B. Intermediate and high Magnus force

In the intermediate Magnus force regime of $0.5 < \alpha_m/\alpha_d < 7.0$, we find the same five phases I, II$_{sb}$, III$_{pl}$, ML, and MC described above, with an expansion of the
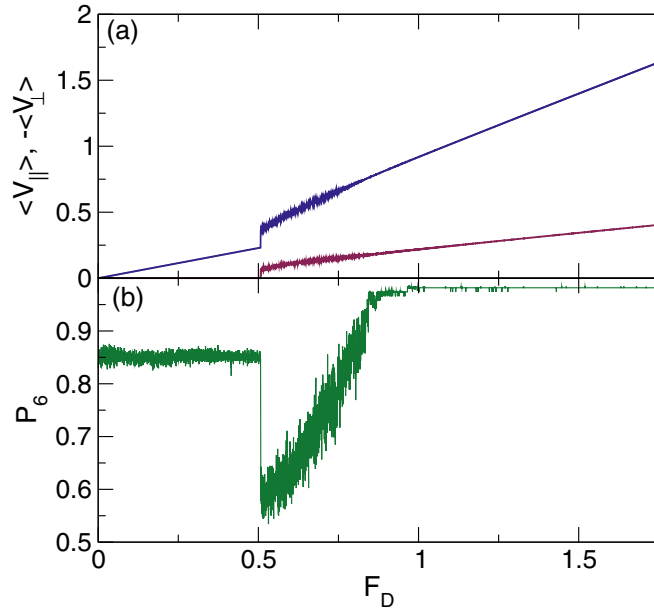
FIG. 12. (a) $\langle V_{\|}\rangle$ (blue) and $-\langle V_{\perp}\rangle$ (red) vs F_D for the system in Fig. 10 with x direction driving at $F_p = 0.75$ and $\alpha_m/\alpha_d = 0.25$. Here we have multiplied $\langle V_{\perp}\rangle$ by -1 for clarity. (b) The corresponding P_6 vs F_D showing the absence of the MS phase.

ML phase since the driving force at which the ML-MC transition occurs increases with increasing Magnus force. We plot $\langle V_{\|}\rangle$ and $\langle V_{\perp}\rangle$ versus F_D in Fig. 14(a) for a system with $\alpha_m/\alpha_d = 6.0$. For clarity, we have normalized $\langle V_{\perp}\rangle$ to the value of $\langle V_{\|}\rangle$ at high drives by dividing $\langle V_{\perp}\rangle$ by α_m/α_d and multiplying it by -1. We can also characterize the dynamic phases by measuring the skyrmion velocity deviations in the x and y directions as in previous work [100,101], $\delta V_{\|} = \sqrt{[\sum_i^N (v_{\|}^i)^2 - \langle V_{\|}\rangle^2]/N}$ and $\delta V_{\perp} =$
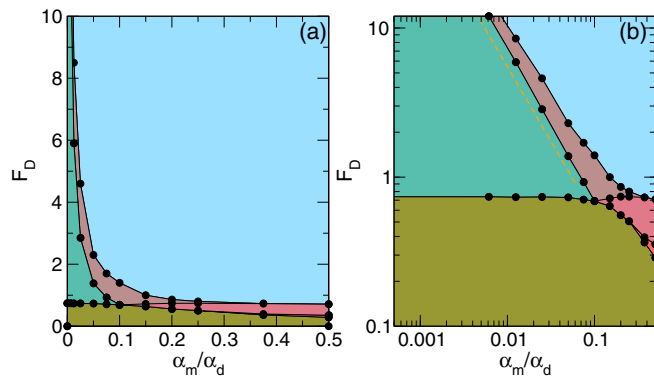

FIG. 13. The dynamic phase diagram as a function of F_D vs α_m/α_d for the low Magnus force regime. Phase I, olive green; moving smectic (MS) phase, teal; moving liquid (ML) phase, brown; plastic flow phase III_{pl}, pink; shear band phase II_{sb}, red; and the moving crystal (MC) phase, light blue. The MS phase occurs only when $\alpha_m/\alpha_d < 0.1$. (b) The same data on a log-log scale. The dashed orange line is a fit to $F_D \propto 1/(\alpha_m/\alpha_d)$, showing that the drives at which the MS-ML and ML-MC phase transitions occur diverge as α_m/α_d decreases.
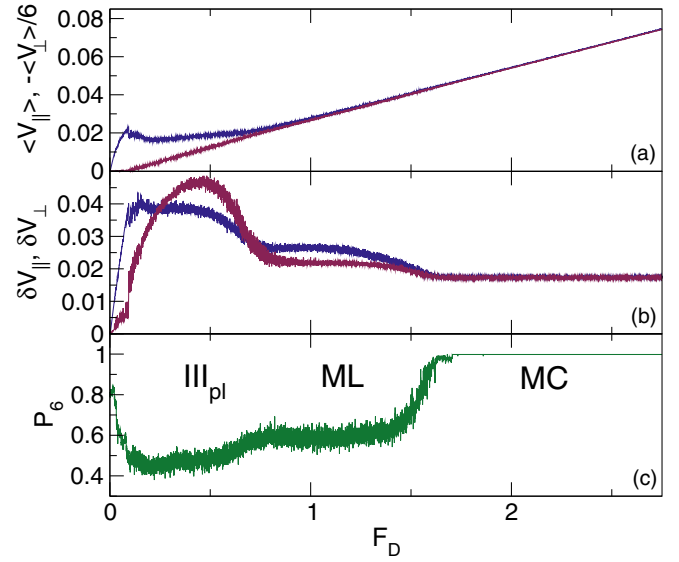

FIG. 14. (a) $\langle V_{\|}\rangle$ (blue) and $-\langle V_{\perp}\rangle/6$ (red) vs F_D for a system with x direction driving at $F_p = 0.75$ and $\alpha_m/\alpha_d = 6.0$. For clarity, we have multiplied $\langle V_{\perp}\rangle$ by -1 and divided it by the value of α_m/α_d in order to normalize $\langle V_{\perp}\rangle$ to the value of $\langle V_{\|}\rangle$ at high drives. (b) The corresponding velocity deviations $\delta V_{\|}$ (blue) and $\delta V_{\perp}$ (red) vs F_D. (c) The corresponding P_6 vs F_D, where we find an extended window of moving liquid (ML) phase. III_{pl}, plastic flow phase; MC, moving crystal phase.

$\sqrt{[\sum_i^N (v_{\perp}^i)^2 - \langle V_{\perp}\rangle^2]/N}$. The plot of $\delta V_{\|}$ and $\delta V_{\perp}$ versus F_D in Fig. 14(b) indicates that the velocity deviations are largest in the plastic flow phase, and diminish to a constant value in the moving crystal phase. In Fig. 14(c) we show P_6 versus F_D for the same system. When $F_D/F_p > 1.0$, we find an extensive region of ML phase in which P_6 has a higher value than in the plastic flow phase but a lower value than in the moving crystal phase.

The shear banding phase II_{sb} disappears when $\alpha_m/\alpha_d > 2.0$, and it is replaced by phase II_a in which skyrmions enter the pinned region via avalanches but where there is almost no flow parallel to the drive. In Fig. 15 we illustrate a system with $\alpha_m/\alpha_d = 2.5$ at $F_D = 0.1$, 0.2, 0.3, and 0.5. The motion in the pinned region at $F_D = 0.1$ and 0.2 in Figs. 15(a) and 15(b) is at almost $90°$ to the drive, while for $F_D = 0.3$ in Fig. 15(c) there is some motion at a lower angle. This effect is similar to what occurs in the Bean state found in superconductors, where vortices enter from the edge of the sample, creating a gradient in the vortex density [79,80]. In the skyrmion case, even though the skyrmion density builds up at the edge of the pinned region, the strong Magnus force suppresses motion in the x direction, parallel to the drive. Eventually when F_D is large enough, skyrmions can travel all the way across the pinned region and the system enters the plastic flow phase III_{pl} as shown in Fig. 15(d) at $F_D = 0.5$. In this work we do not characterize the statistics of the avalanches in phase II_a; however, previous work on skyrmion avalanches for density gradient driven skyrmions analyzed the avalanches in terms of a critical phenomenon [100], and since we have a similar density gradient in our system, we expect that the avalanche statistics should be similar. The motion of skyrmions in the
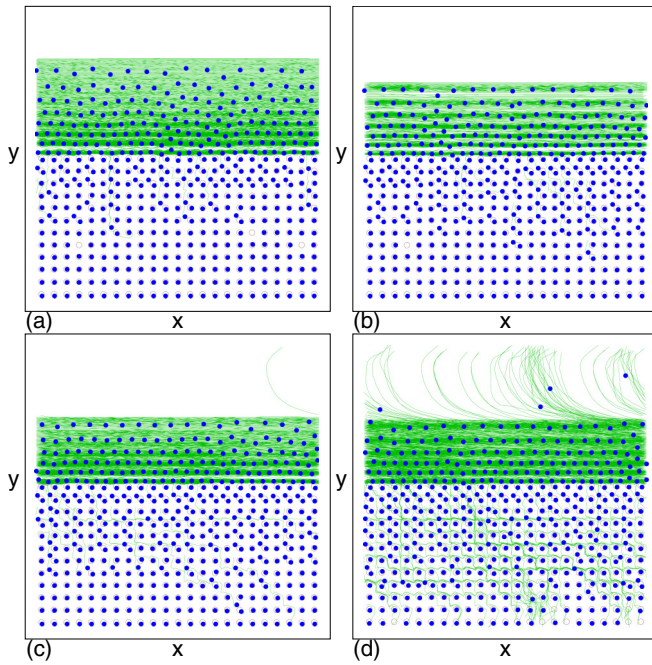
FIG. 15. Skyrmion locations (blue dots), pinning site locations (open circles), and skyrmion trajectories (green lines) during a fixed time interval for a system with x direction driving at $F_p = 0.75$ and $\alpha_m/\alpha = 2.5$, where the shear banding phase is replaced with the avalanche phase II_a. Moving skyrmions from the unpinned region enter the pinned region in the form of avalanches at (a) $F_D = 0.1$, (b) $F_D = 0.2$, and (c) $F_D = 0.3$. (d) The plastic flow phase III_{pl} at $F_D = 0.5$.

FIG. 16. $\langle V_{||} \rangle$ (blue) and $\langle V_\perp \rangle$ (red) vs F_D in a sample with x direction driving at $F_p = 0.75$ and $\alpha_m/\alpha_d = 10$. Above phase II_a, there is a region of large oscillations in the intermittent phase I_{in}, where large-scale phase-separated flow occurs as shown in Fig. 17.

$-x$ direction at the top of Fig. 15(d) is a result of the combination of the Magnus force with the repulsion from the skyrmions in the pinned region. As a skyrmion exits the pinned region and enters the field of view at the top of the panel, it is experiencing both the driving force F_D oriented in the x direction and a repulsion oriented in the $-y$ direction from the skyrmions that are still trapped in the pinned region. Close to the edge of the pinned region, the repulsive force is dominant and the net force acting on the skyrmion is oriented almost entirely in the $-y$ direction. As a result, the Magnus force acting on the skyrmion is oriented partially in the $-x$ direction, and when α_m/α_d is sufficiently large, the skyrmion has a noticeable component of its motion opposite to the direction of the applied drive. As the skyrmion moves further away from the edge of the pinned region, the repulsion from the trapped skyrmions diminishes and the net force acting on the skyrmion gradually rotates out of the $-y$ direction towards the x direction. The corresponding Magnus force rotates away from the $-x$ direction towards the $-y$ direction. The result is the curved trajectories that appear in Fig. 15(d).

For $\alpha_m/\alpha_d > 7.0$ we observe a new phenomenon in which a portion of the plastic flow phase develops strong intermittency, with skyrmion flow occurring in large-scale phase-separated moving channels in the pinned region. These channels change in shape and size as a function of time, producing strong oscillations in the velocity. In Fig. 16 we plot $\langle V_{||} \rangle$ and $\langle V_\perp \rangle$ versus F_D for a sample with $\alpha_m/\alpha_d = 10$. Here, after the initial phase II_a, in phase I_{in} there are strong oscillations in
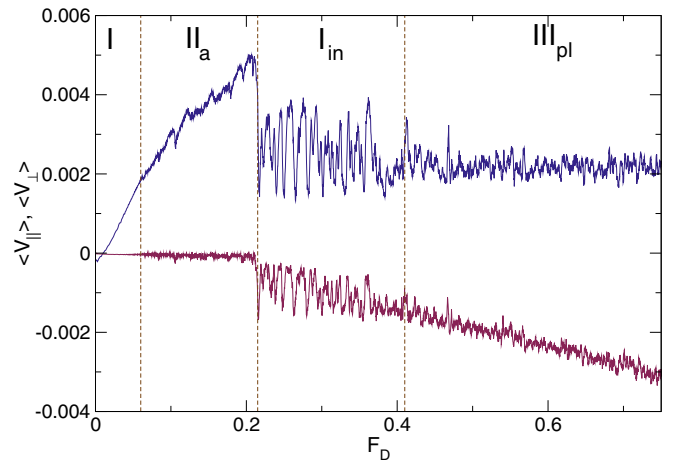
the velocity both parallel and perpendicular to the drive which decrease in amplitude until the sample enters phase III_{pl} at $F_D = 0.42$. In Fig. 17 we highlight the skyrmion motion in phase I_{in}. At $F_D = 0.12$, Fig. 17(a) shows that a channel has formed along which the skyrmions enter the pinned region at nearly $90°$ to the driving direction. Several instances of spiraling motion of individual skyrmions appear, which are indicative of the large value of the Magnus force. In Fig. 17(b) the same system at $F_D = 0.25$ contains a phase separated
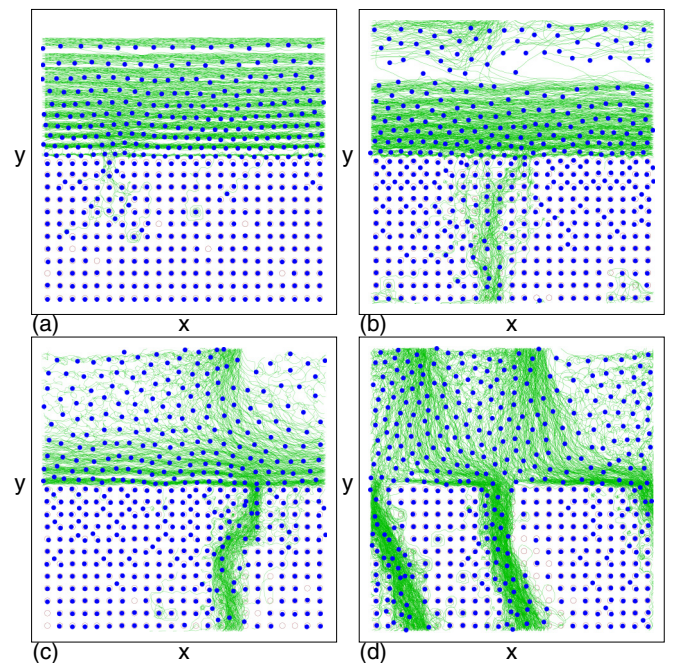

FIG. 17. Skyrmion locations (blue dots), pinning site locations (open circles), and skyrmion trajectories (green lines) during a fixed time interval for the system in Fig. 16 with x direction driving at $F_p = 0.75$ and $\alpha_m/\alpha_d = 10$ in phase I_{in}. (a) $F_D = 0.12$, (b) $F_D = 0.25$, (c) $F_D = 0.3185$, and (d) $F_D = 0.325$.
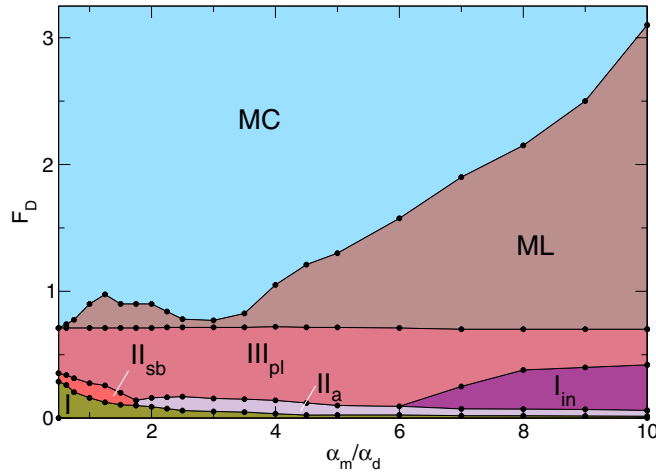
FIG. 18. The dynamic phase diagram as a function of F_D vs α_m/α_d in samples with x direction driving at $F_p = 0.75$, showing phases I (olive green), II$_{sb}$ (red), III$_{pl}$ (pink), II$_a$ (light purple), I$_{in}$ (violet), ML (brown), and MC (blue). Here phase II$_a$ appears when $\alpha_m/\alpha_d > 1.9$ and phase I$_{in}$ appears when $\alpha_m/\alpha_d \geqslant 7.0$.
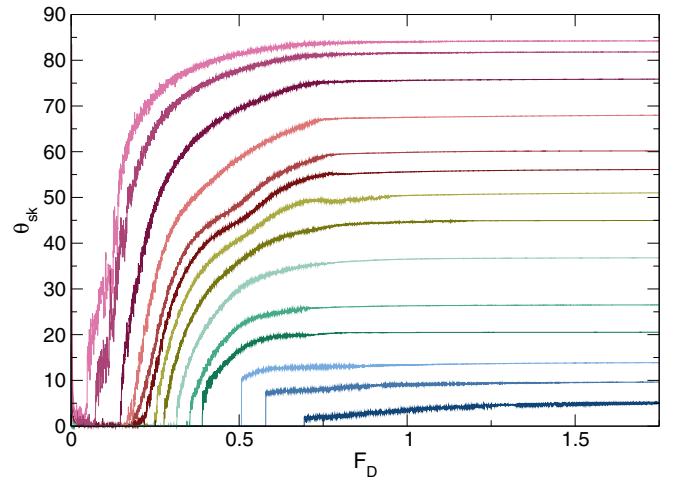

FIG. 19. The evolution of θ_{sk} vs F_D for samples with x direction driving at $F_p = 0.75$ and $\alpha_m/\alpha_d = 10, 7, 5, 2.5, 1.75, 1.25, 1.0, 0.75, 0.7, 0.5, 0.375, 0.25, 0.175,$ and 0.125, from top to bottom.

flow confined to a single river moving at $-90°$ to the driving direction through the pinned region. At $F_D = 0.3185$ and 0.325 in Figs. 17(c) and 17(d), the large-scale rivers change position as a function of both time and drive, and the large spike in $\langle V_\parallel \rangle$ in Fig. 16 corresponds to two or three flowing rivers, while the minimum corresponds to one flowing river. As F_D increases, more of these rivers begin to flow, and when the system enters phase III$_{pl}$, the flow is disordered but uniform. Phase segregation dynamics has been observed previously in the particle-based model when both α_m/α_d and the pinning strength are large [100]. Continuum-based simulations also show that dynamical segregation effects can occur when the pinning strength is sufficiently large [34]. When the drive is large enough, the effect of the pinning is reduced and the dynamical behavior becomes more uniform. We observe the intermittent phase I$_{in}$ for α_m/α_d as high as 30, which is the largest value we considered. In general, the phase-separated dynamics or intermittency occurs only when $F_D/F_p < 1.0$. The segregation occurs since when the Magnus force is large, skyrmions that are close together tend to spiral around one another rather than moving apart. In regions where the skyrmion density is largest, the pinning effectiveness is reduced, leading to additional flow in the same location.

In Fig. 18 we highlight the dynamic phase diagram as a function of F_D versus α_m/α_d for the intermediate and high Magnus force regimes of $0.5 \leqslant \alpha_m/\alpha_d \leqslant 10$. Here the shear banding phase II$_{sb}$ occurs for $0.5 < \alpha_m/\alpha_d \leqslant 1.9$, but is replaced by phase II$_a$ for $\alpha_m/\alpha_d > 1.9$. When $\alpha_m/\alpha_d > 7.0$, a window of phase I$_{in}$ appears between phases II$_a$ and III$_{pl}$. The driving force at which the ML-MC transition occurs increases with increasing α_m/α_d when $\alpha_m/\alpha_d > 3$. The increase in the width of the ML phase as α_m/α_d increases occurs since higher values of α_m produce more motion associated with the nondissipative Magnus force, which creates spiraling motion of the skyrmions when they interact with the pinning sites.

In Fig. 19 we show the evolution of the skyrmion Hall angle θ_{sk} versus F_D for varied α_m/α_d ranging from 0.125 to

10. In each case, θ_{sk} starts at zero when $F_D = 0$ and increases with increasing F_D in the plastic flow phase. There is a smaller increase in θ_{sk} with increasing F_D in the ML phase, and θ_{sk} reaches a saturation value in the MC phase. Another interesting effect is that θ_{sk} changes discontinuously when $\theta_{sk} < 15°$.

IV. VARIED PINNING STRENGTH

We next consider the effect of varying the pinning strength F_p while holding the ratio of the Magnus force to the damping term fixed at $\alpha_m/\alpha_d = 1.0$. The behavior can be divided into three regimes depending on whether the pinning is weak, intermediate, or strong.

The weak pinning regime appears when $F_p < 0.05$. Here the motion is elastic and each skyrmion keeps its same neighbors for all values of F_D. At low drives we find a pinned phase P in which the skyrmions in the pinned region are able to prevent the skyrmions in the unpinned region from moving due to the skyrmion-skyrmion interaction forces. As the drive increases, an elastic depinning transition occurs into a moving lattice phase with a finite skyrmion Hall angle, as shown in Fig. 20(a) where we plot $\langle V_\parallel \rangle$ and $\langle V_\perp \rangle$ versus F_D. Figure 20(b) shows the corresponding P_6 versus F_D curve, which changes only slightly at the depinning transition from the coexisting pinned squares and hexagonal lattice into a moving lattice. When the pinning is even weaker, there is a transition in the pinned state from a pinned square lattice to a floating triangular lattice, and the depinning threshold drops even further. For $F_p > 0.03$, we observe a separate depinning transition of the skyrmions in the unpinned region which move at zero Hall angle, followed by a plastic flow region and a moving crystal regime. In Fig. 21 we show the dynamic phase diagram in the weak pinning regime as a function of F_D versus F_p where we highlight the pinned phase P, moving crystal MC, phase I motion, and the plastic flow state III$_{pl}$.

In the intermediate pinning regime $0.05 < F_p < 3.5$, we observe phases I and III$_{pl}$ as well as the MC state. At $\alpha_m/\alpha_d = 1.0$, the intrinsic skyrmion Hall angle is $\theta_{sk}^{int} = 45°$, which
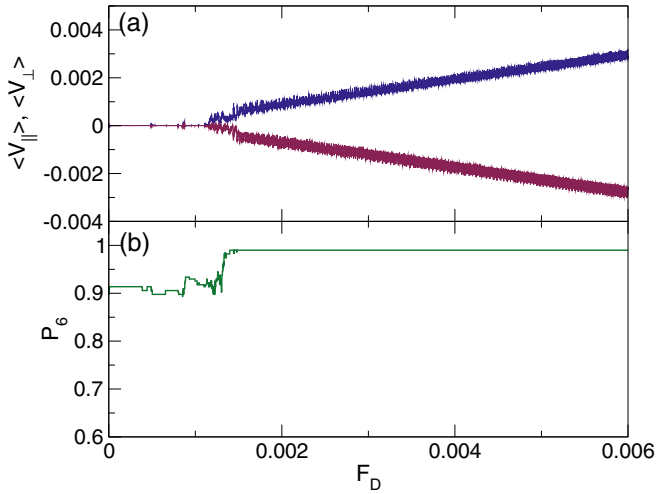
FIG. 20. A system with x direction driving at $\alpha_m/\alpha_d = 1.0$ and $F_p = 0.01$, where an elastic depinning transition in which the skyrmions keep their same neighbors separates the pinned phase P from the MC phase. (a) $\langle V_{||}\rangle$ (blue) and $\langle V_\perp\rangle$ (red) vs F_D. (b) The corresponding P_6 vs F_D.

corresponds to a locking direction of the square pinning array in the pinned portion of the sample. For $F_p < 0.85$, the elastic energy associated with the triangular skyrmion lattice in the MC state is large enough that the skyrmion motion does not lock with the pinning lattice; however, as the pinning strength increases, we find a regime in which the pinning can induce a directional locking, as indicated by the formation of a square moving skyrmion lattice of the type shown in Fig. 5(f). In Fig. 22(a) we plot $\delta V_{||}$ and $\delta V_\perp$ versus F_D for a sample with $F_p = 0.8$, highlighting the formation of the triangular MC phase followed by a transition to the square moving crystal phase MC_{sq}. Within the MC phase, occasional small rotations of the triangular lattice occur which produce the jumps in in $\delta V_\perp$. At $F_p = 1.0$, the $\delta V_{||}$ and $\delta V_\perp$ versus F_D curves in Fig. 22(b) indicate that the transition to the MC_{sq} state has
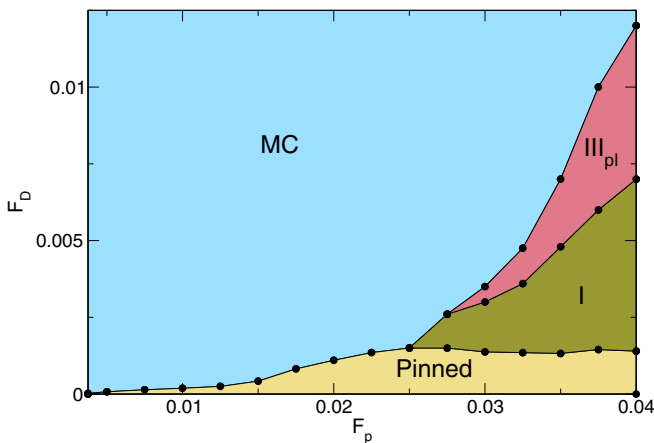

FIG. 21. Dynamic phase diagram as a function of F_D vs F_p in the weak pinning regime for samples with x direction driving and $\alpha_m/\alpha_d = 1.0$, showing the pinned phase (yellow), moving crystal MC (light blue), plastic flow III_{pl} (pink), and phase I (olive green).
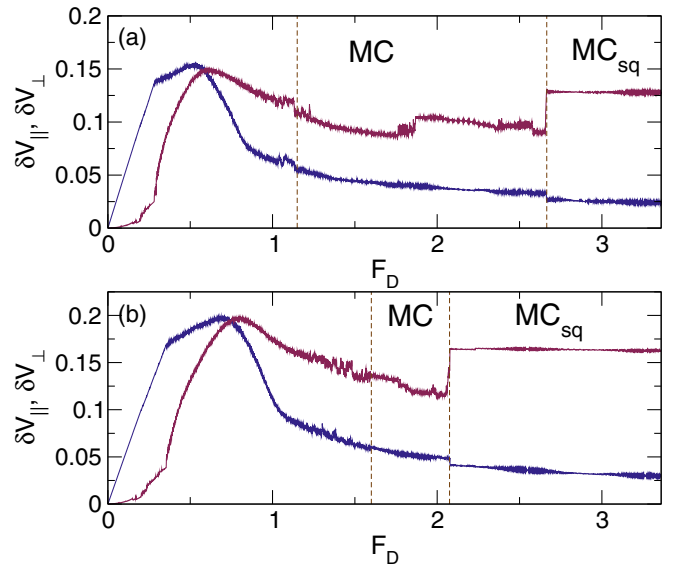

FIG. 22. Velocity deviations $\delta V_{||}$ (blue) and $\delta V_\perp$ (red) vs F_D for samples with x direction driving and $\alpha_m/\alpha_d = 1.0$ showing a transition from a triangular moving crystal MC to a square moving crystal MC_{sq}. (a) $F_p = 0.8$. (b) $F_p = 1.0$.

shifted to lower drives. For smaller values of F_p, the MC phase disappears and there is a transition directly from a ML phase to the MC_{sq} phase.

In Figs. 23(a) and 23(b) we show a blowup of the skyrmion Hall angle θ_{sk} versus F_D across the ML-MC-MC_{sq} transitions for the system in Fig. 22 at $F_p = 0.8$ and $F_p = 1.0$, respectively. Here, θ_{sk} is lower in the MC phase than in the MC_{sq} phase. At $F_p = 0.8$ in Fig. 23(a), the onset of the MC phase coincides with a flattening of θ_{sk}, but as F_D increases, several jumps in θ_{sk} occur due to large-scale rotations of the moving lattice, and finally in the MC_{sq} state the jumps in θ_{sk} disappear.

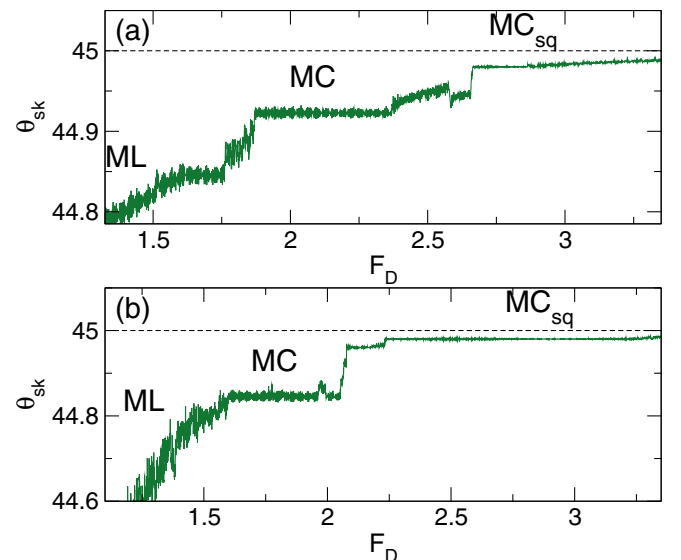FIG. 23. θ_{sk} vs F_D showing the evolution of the skyrmion Hall angle across the ML-MC-MC_{sq} transitions for the system in Fig. 21 with x direction driving and $\alpha_m/\alpha_d = 1.0$. (a) $F_p = 0.8$. (b) $F_p = 1.0$.
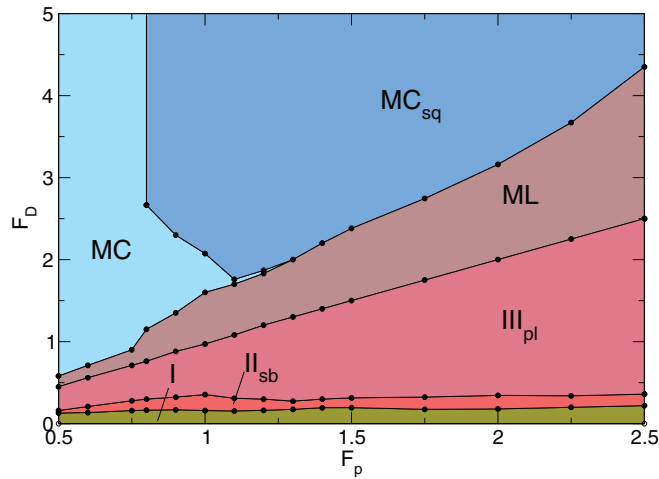
FIG. 24. Dynamic phase diagram as a function of F_D vs F_p for the intermediate pinning regime in samples with x direction driving and $\alpha_m/\alpha_d = 1.0$ showing phases I (olive green), II$_{sb}$ (red), III$_{pl}$ (pink), ML (brown), MC (light blue), and MC$_{sq}$ (dark blue).

The angle of motion in the MC$_{sq}$ is slightly smaller than 45° due to a weak guiding effect of the skyrmions along the boundaries separating the pinned and unpinned regions of the sample.

In Fig. 24 we construct a dynamic phase diagram as a function of F_D versus F_p for the intermediate pinning regime, highlighting phases I, II$_{sb}$, III$_{pl}$, ML, MC, and MC$_{sq}$. We note that there is still a pinned phase P at small F_D; however, on the scale of the figure this phase cannot be seen. The MC-MC$_{sq}$ transition shifts to higher values of F_D as the pinning strength is lowered. We have also examined varied α_m/α_d for different pinning strengths and find similar phases to those shown in Fig. 24; however, the MC$_{sq}$ phase appears only when α_m/α_d is near 1.0. An intermittent phase I$_{in}$ appears for low values of α_m/α_d when F_p is large.

As F_p increases, we find wider windows of F_D in which θ_{sk} is small and gradually increasing. When $F_p > 3.0$, we start to observe the trapping of multiple skyrmions in individual pinning sites, which causes the appearance of intervals of F_D in which $\langle V_\| \rangle$ *decreases* with increasing F_D. This phenomenon is known as negative differential conductivity since $d\langle V_\| \rangle/dF_D < 0$, as illustrated in Fig. 25(a) where we plot $\langle V_\| \rangle$ and $\langle V_\perp \rangle$ versus F_D for a system with $F_p = 4.5$ and $\alpha_m/\alpha_d = 1.0$. Figure 26 shows the skyrmion positions in this sample at $F_D = 1.0$, just after the drop in $\langle V_\| \rangle$, where multiple skyrmions can be trapped at individual pinning sites and where there is an increase in the skyrmion density along the boundary of the pinned region. In earlier work where the number of skyrmions was much smaller than the number of pinning sites, we also observed negative mobility that arises when the skyrmions in the unpinned region are forced into the pinned region and become immobile [81]. A similar phenomenon can occur at higher skyrmion densities when multiple skyrmions are trapped by each pinning site. We also find signatures of multiple regimes in θ_{sk}, as shown in Fig. 25(b). The $\langle V_\| \rangle$, $\langle V_\perp \rangle$, and θ_{sk} versus F_D curves for a system with $\alpha_m/\alpha_d = 4.0$ appear in Figs. 25(c) and 25(d), highlighting the
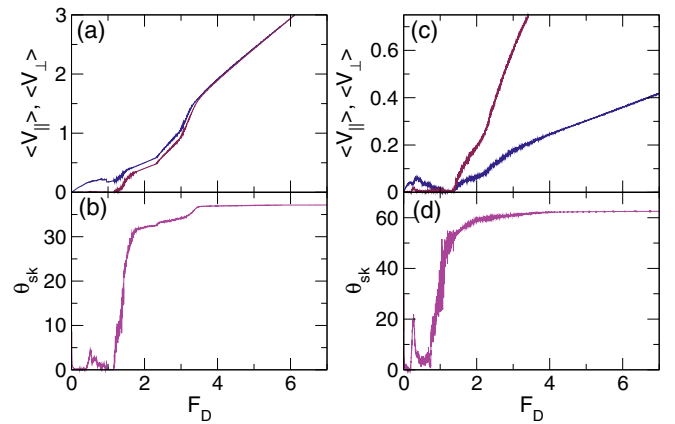

FIG. 25. (a) $\langle V_\| \rangle$ (blue) and $\langle V_\perp \rangle$ (red) vs F_D for a sample with x direction driving, $\alpha_m/\alpha_d = 1.0$, and $F_p = 4.5$ showing regions in which $d\langle V_\| \rangle/dF_D < 0.0$, also known as negative differential mobility, due to the trapping of multiple skyrmions by individual pinning sites. (b) The corresponding θ_{sk} vs F_D where multiple regimes appear. (c) $\langle V_\| \rangle$ and $\langle V_\perp \rangle$ vs F_D for a sample with x direction driving, $\alpha_m/\alpha_d = 4.0$, and $F_p = 4.5$. (d) The corresponding θ_{sk} vs F_D.

persistence of the negative differential mobility effect even for large intrinsic skyrmion Hall angles.

V. DRIVING PERPENDICULAR TO THE PINNING STRIP

We next consider the effect of applying a drive along the y direction, perpendicular to the pinning strip. In an overdamped system, such a drive would push the particles into the pinned region, while for skyrmions, the Magnus force will
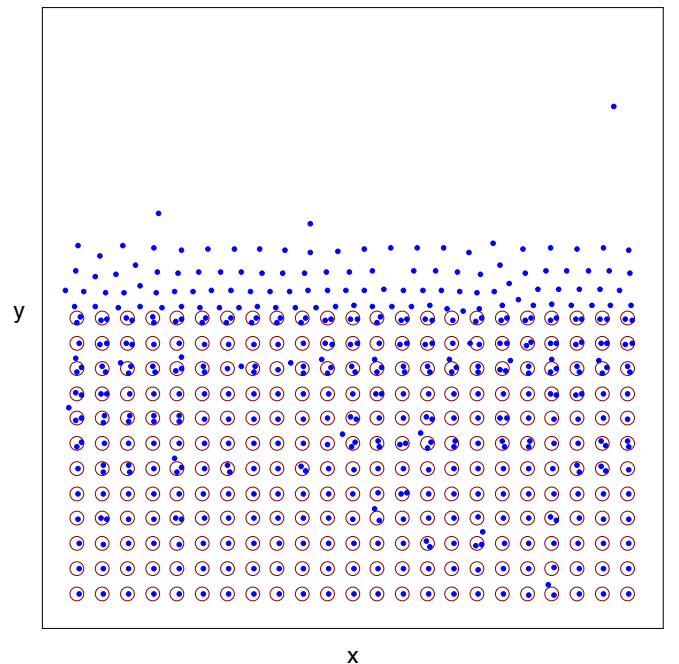

FIG. 26. Skyrmion locations (blue dots) and pinning site locations (open circles) for the system in Fig. 25(a) with x direction driving at $\alpha_m/\alpha_d = 1.0$ and $F_p = 4.5$ for $F_D = 1.0$, just after the drop down in $\langle V_\| \rangle$, showing multiple skyrmion trapping by individual pinning sites.
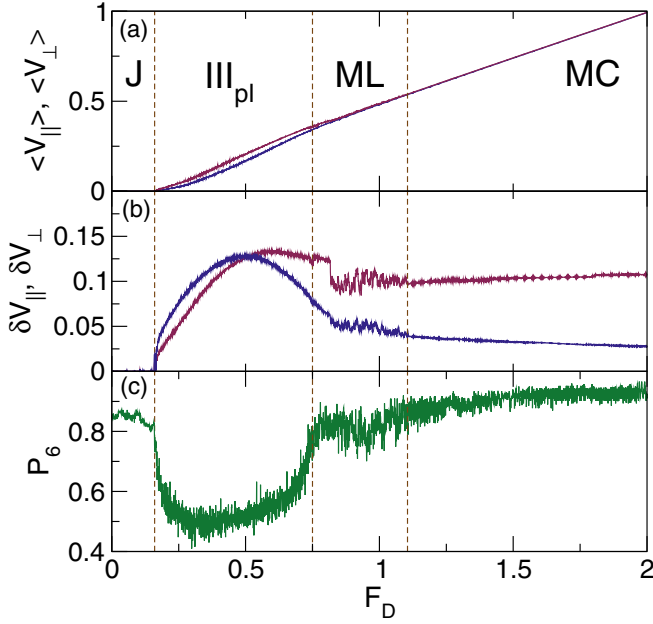
FIG. 27. Driving in the y direction, perpendicular to the pinning strip, for the system in Fig. 2 with $F_p = 0.75$ and $\alpha_m/\alpha_d = 1.0$. The vertical dashed lines denote transitions among a jammed phase J, a moving plastic flow phase III$_{pl}$, a ML, and a MC$_{sq}$ phase. (a) $\langle V_{||} \rangle$ (blue) and $\langle V_\perp \rangle$ (red) vs F_D. (b) $\delta V_{||}$ (blue) and $\delta V_\perp$ (red) versus F_D. (c) P_6 vs F_D. Velocities are always measured parallel or perpendicular to the direction of the pinning strip.
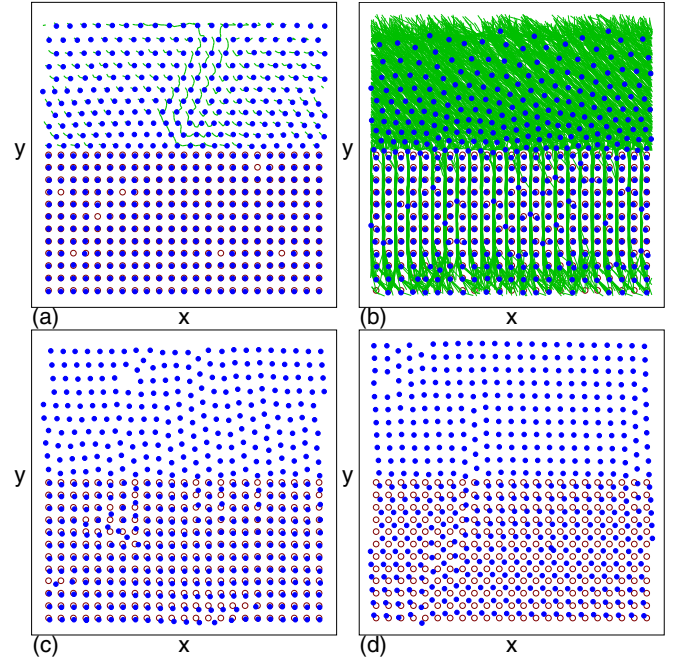

FIG. 28. Skyrmion locations (blue dots), pinning site locations (open circles), and skyrmion trajectories (green lines) during a fixed time interval for the system in Fig. 27 with y direction driving, $F_p = 0.75$, and $\alpha_m/\alpha_d = 1.0$. (a) Transient rearrangements in the jammed phase J at $F_D = 0.06$. (b) Phase III$_{pl}$ at $F_D = 0.25$, where the skyrmions can cross the entire system. (c) The ML phase at $F_D = 1.0$, showing the skyrmion locations only. (d) The moving square lattice MC$_{sq}$ phase at $F_D = 1.5$ showing the skyrmion locations only.

also generate motion of the particles parallel to the pin-free channel. In general, we observe a jamming behavior in which the skyrmions are pushed into the pinned region but there is no steady-state motion in either direction so that $\langle V_{||} \rangle = \langle V_\perp \rangle = 0$. In Fig. 27(a) we plot $\langle V_\perp \rangle$ and $\langle V_{||} \rangle$ versus F_D for a sample with $F_p = 0.75$ and $\alpha_m/\alpha_d = 1.0$ with y direction driving. As always, the parallel velocity is measured in the x direction, parallel to the orientation of the pinning strip, so here $\langle V_\perp \rangle$ shows motion in the direction of the applied drive. We find a jammed phase J with $\langle V_{||} \rangle = \langle V_\perp \rangle = 0$ for $F_D < 0.16$. The jammed phase J is distinct from the pinned phase P described earlier. In phase P, pinning results from the finite shear modulus of the skyrmion lattice, while in phase J, pinning arises due to the finite compression modulus of the skyrmion lattice. Since the compression modulus is much larger than the shear modulus, the jammed phase appears over a much larger range of external drives compared to the pinned phase. Within the jammed phase, temporary rearrangements or avalanches occur under increasing F_D as the skyrmions adjust their positions to accommodate the drive, as shown in Fig. 28(a) at $F_D = 0.06$. In Fig. 27(b) we plot $\delta V_{||}$ and $\delta V_\perp$ versus F_D. Both quantities become finite in phase III$_{pl}$ when the skyrmions are first able to travel all the way across the pinned region, as illustrated in Fig. 28(b) at $F_D = 0.25$. In Fig. 27(c), the P_6 versus F_D curve has a drop across the J-III$_{pl}$ transition. As F_D is further increased, the flow becomes more disordered. For $0.75 < F_D < 1.1$, all the skyrmions are moving and the system forms a ML phase as shown in Fig. 28(c) at $F_D = 1.0$. There is an increase in P_6 up to $P_6 = 0.8$ in the ML phase, and we find strong fluctuations in the velocity deviations $\delta V_{||}$ and

$\delta V_\perp$ for $0.75 < F_D < 1.1$. Above $F_D = 1.1$, the system enters a moving square crystal phase MC$_{sq}$, illustrated in Fig. 28(d). The ML-MC$_{sq}$ transition is visible as a shift in P_6 and a reduction of the fluctuations in $\delta V_{||}$ and $\delta V_\perp$.

We find different regimes of behavior for driving in the perpendicular direction depending on whether α_m/α_d is small or large. In Fig. 29(a) we plot $\langle V_{||} \rangle$ and $\langle V_\perp \rangle$ for a system with $\alpha_m/\alpha_d = 0.0125$, where we have normalized $\langle V_{||} \rangle$ by dividing it by α_m/α_d. Figures 29(b) and 29(c) show the corresponding $\delta V_{||}$, $\delta V_\perp$, and P_6 versus F_D curves. In this case, we find a jammed phase J and a plastic flow phase III$_{pl}$ in addition to a new phase which we call a partially locked (PL) state. Here, the motion of the skyrmions within the pinned region is completely locked in the y direction, parallel to the drive, but the skyrmions in the unpinned region move at an angle to the drive. The III$_{pl}$-PL phase transition is associated with an increase in P_6 and a drop in $\langle V_{||} \rangle$. In phase III$_{pl}$, skyrmions are moving in both the x and y directions; however, in the PL phase, skyrmions in the pinned region move only in the y direction, causing the value of $\langle V_{||} \rangle$ to drop. In Fig. 30(a) we show the Voronoi construction for the skyrmion locations in the PL phase at $F_D = 1.0$. Within the pinned region, the skyrmion lattice is aligned with the y direction, while in the unpinned region, it is aligned at an angle to the y direction. Near $F_D = 2.0$ in Fig. 29, there is a transition to a MC phase in which the skyrmion motion is no longer locked to the y direction, as indicated by a jump up in $\langle V_{||} \rangle$ and a cusp in $\delta V_{||}$ and $\delta V_\perp$. There is also a small dip in P_6 near the PL-
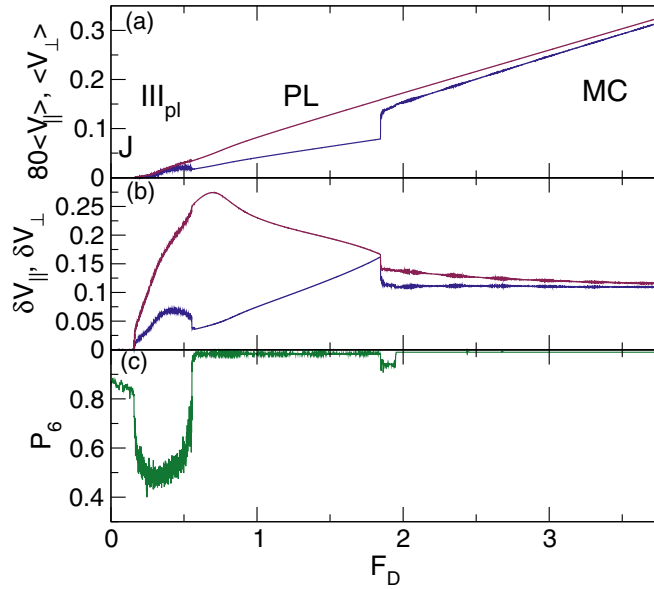
FIG. 29. (a) $80\langle V_{\parallel}\rangle$ (blue) and $\langle V_{\perp}\rangle$ (red) vs F_D for the system with y direction driving at $\alpha_m/\alpha_d = 0.0125$ and $F_p = 0.75$. For clarity, we have divided $\langle V_{\parallel}\rangle$ by the value of α_m/α_d in order to normalize $\langle V_{\parallel}\rangle$ to the value of $\langle V_{\perp}\rangle$ at high drives. (b) The corresponding $\delta V_{\parallel}$ (blue) and $\delta V_{\perp}$ (red) vs F_D. (c) The corresponding P_6 vs F_D. We observe a jammed phase (J), plastic flow phase (III$_{pl}$), partially locked phase (PL), and a moving crystal phase (MC).

MC transition. Figure 30(b) shows the Voronoi construction of the skyrmion locations in the MC phase at $F_D = 2.5$, where the entire skyrmion lattice is aligned in the same direction. The PL phase is produced by the locking of the skyrmion motion along the symmetry direction of the pinning lattice, but when α_m/α_d is large enough, the partially locked phase is replaced by the moving crystal phase.

In Fig. 31 we construct a dynamic phase diagram as a function of F_D versus α_m/α_d for driving in the y direction. The PL phase appears when $\alpha_m/\alpha_d < 0.4$ and diverges in width
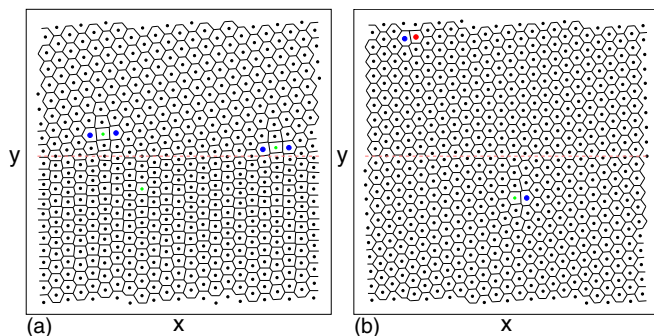

FIG. 30. The Voronoi construction for the skyrmion locations for the system in Fig. 29 with y direction driving, $F_p = 0.75$, and $\alpha_m/\alpha_d = 0.0125$. The red dashed line indicates the edge of the pinned region. (a) The PL phase at $F_D = 1.0$, where there is a change in the orientation of the crystal across the boundaries separating the unpinned and pinned regions. (b) The MC phase at $F_D = 2.5$. The dislocation pair in the pinned region is in the process of gliding and temporarily has more than seven neighbors on one end.
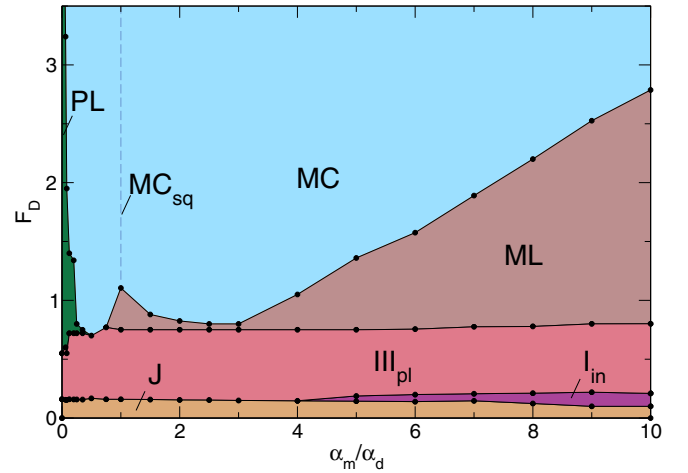

FIG. 31. Dynamic phase diagram as a function of F_D vs α_m/α_d for driving in the y direction for a system with $F_p = 0.75$. Partially locked phase (PL), dark green; jammed phase (J), tan; plastic flow (III$_{pl}$), pink; intermittent (I$_{in}$), violet; moving liquid (ML), brown; moving crystal (MC), light blue. At $\alpha_m/\alpha_d = 1.0$ there is a moving square lattice (MC$_{sq}$), dark blue dashed line.

as α_m/α_d goes to zero. At low drives, the jammed phase J occurs for all α_m/α_d, and is followed at higher drives by an intermittent avalanche phase I$_{in}$ when $\alpha_m/\alpha_d \geqslant 5.0$. The I$_{in}$ phase is similar to that found for driving in the x direction but its onset is at somewhat lower values of α_m/α_d. We find the plastic phase III$_{pl}$ for all values of α_m/α_d, and the ML phase increases in extent with increasing Magnus force, similar to the behavior of the ML phase in the system with x direction driving. At $\alpha_m/\alpha_d = 1.0$, there is a transition from the ML into a moving square lattice rather than to a moving crystal phase. It is possible that for α_m/α_d near 1.0, there could be a regime in which the moving square lattice transitions into the moving crystal phase, with the value of F_D at which the transition occurs diverging at $\alpha_m/\alpha_d = 1.0$. For fixed α_m/α_d and increasing F_p, we observe a similar evolution of the phases as in the system with x direction driving, including a transition to elastic depinning for small F_p.

VI. DISCUSSION

Our results should be general for skyrmion systems with some form of inhomogeneous pinning. Although we specifically focus on the case of a square lattice of pinning sites, we expect similar results to appear if the pinned region contains randomly placed pinning sites or a triangular pinning lattice. One exception to this is that the strong guidance effects that occur for skyrmion Hall angles of $\theta_{sk}^{int} = 45°$ would not appear for most other pinning geometries since these are specific to the square pinning lattice. In this work we did not consider hysteretic effects, but it is likely that many of the phases would show hysteresis while others would not. There is now evidence for a variety of skyrmion systems that exhibit thermal effects or diffusion, so it would be interesting to study how temperature could affect the results, such as by inducing creep. It may also be possible to measure the evolution of the shear modulus with temperature. For instance, at low drives

there is a pinned phase in which the skyrmions trapped at the pinning sites hold back the skyrmions in the pin-free region, and this can only occur if the skyrmion lattice has a finite shear modulus. As the temperature increases, the shear modulus would be reduced before vanishing at the melting transition, which would destroy the indirect pinning of the skyrmions in the pin-free region, causing them to flow. Similar effects have been studied in the context of superconducting vortices driven through weak pinning channels. Although our work involves skyrmions, many of these results could be relevant to other systems even in the absence of a Magnus force. Some examples include vortices or colloids in a system with a combination of strong and weak pinning where the direction of the drive is not fixed but gradually changes, which could mimic the effect of the changing skyrmion Hall angle.

VII. SUMMARY

We have numerically examined the dynamics of skyrmions in systems with inhomogeneous pinning. We focus on a sample containing a strip of square pinning coexisting with a region of no pinning. When the external drive is parallel to the pinning strip, we find that initially, only the skyrmions in the unpinned region flow, termed phase I motion, and that at higher drives, a shear banding phase II_{sb} emerges in which flow occurs in the pinned region with a velocity gradient. Both of these phases have a skyrmion Hall angle of zero. When the drive is strong enough, the skyrmions enter the plastic motion or disordered phase III_{pl} in which the skyrmion Hall angle becomes finite. At higher drives, there is a moving liquid (ML) phase followed by a transition into a moving crystal (MC). The skyrmion Hall angle increases most rapidly with increasing drive in the plastic flow phase, and increases more slowly in the ML phase. For phases I, II_{sb}, and III_{pl}, there is an accumulation of skyrmions along the edge of the pinned region due to the Magnus force, which pushes the skyrmions in the unpinned region toward the pinned region. As the strength of the Magnus force increases, there is a phase in which

the skyrmions enter the pinned region under avalanche-like transport, creating a density gradient similar to the Bean state found in type-II superconductors. There is also an intermittent or dynamically phase-separated state in which the skyrmion motion through the pinned region is confined to localized rivers that change in size and location with increasing drive. For weak Magnus forces, we find a smectic phase in which the skyrmion motion is locked in the direction of the drive over an extended range of driving forces, followed by a transition to a state in which the skyrmion Hall angle is finite. For weak pinning, the system exhibits an elastic pinning regime with a shear jammed state at low drives followed at higher drives by a moving crystal phase in which each skyrmion keeps its same neighbors as it moves. When the pinning is strong, we observe negative differential conductivity when skyrmions in the pin-free channel are pushed into the pinned region and become immobile, dropping the overall mobility of the system. When the external drive is perpendicular to the pinning strip, we find a jammed phase at low drives in which skyrmions in the unpinned region are unable to move into the pinned region. As the drive increases, there is a partially locked phase, a moving liquid state, and a moving crystal phase. We show how the transitions between these different phases produce signatures in the skyrmion mobility, coordination numbers, velocity deviations, and global skyrmion lattice structure. Beyond skyrmions, our results could also be relevant for other systems in which Magnus forces can arise, such as vortices in superconductors or superfluids as well as in chiral active matter systems.

[1] S. Mühlbauer, B. Binz, F. Jonietz, C. Pfleiderer, A. Rosch, A. Neubauer, R. Georgii, and P. Böni, Skyrmion lattice in a chiral magnet, Science **323**, 915 (2009).

[2] X. Z. Yu, Y. Onose, N. Kanazawa, J. H. Park, J. H. Han, Y. Matsui, N. Nagaosa, and Y. Tokura, Real-space observation of a two-dimensional skyrmion crystal, Nature (London) **465**, 901 (2010).

[3] N. Nagaosa and Y. Tokura, Topological properties and dynamics of magnetic skyrmions, Nat. Nanotechnol. **8**, 899 (2013).

[4] S. Woo, K. Litzius, B. Krüger, M.-Y. Im, L. Caretta, K. Richter, M. Mann, A. Krone, R. M. Reeve, M. Weigand, P. Agrawal, I. Lemesh, M.-A. Mawass, P. Fischer, M. Kläui, and G. S. D. Beach, Observation of room-temperature magnetic skyrmions and their current-driven dynamics in ultrathin metallic ferromagnets, Nat. Mater. **15**, 501 (2016).

[5] A. Soumyanarayanan, M. Raju, A. L. G. Oyarce, A. K. C. Tan, M.-Y. Im, A. P. Petrovic, P. Ho, K. H. Khoo, M. Tran, C. K. Gan, F. Ernult, and C. Panagopoulos, Tunable room-

temperature magnetic skyrmions in Ir/Fe/Co/Pt multilayers, Nat. Mater. **16**, 898 (2017).

[6] A. Fert, N. Reyren, and V. Cros, Magnetic skyrmions: advances in physics and potential applications, Nat. Rev. Mater. **2**, 17031 (2017).

[7] T. Schulz, R. Ritz, A. Bauer, M. Halder, M. Wagner, C. Franz, C. Pfleiderer, K. Everschor, M. Garst, and A. Rosch, Emergent electrodynamics of skyrmions in a chiral magnet, Nat. Phys. **8**, 301 (2012).

[8] X. Z. Yu, N. Kanazawa, W. Z. Zhang, T. Nagai, T. Hara, K. Kimoto, Y. Matsui, Y. Onose, and Y. Tokura, Skyrmion flow near room temperature in an ultralow current density, Nat. Commun. **3**, 988 (2012).

[9] J. Iwasaki, M. Mochizuki, and N. Nagaosa, Universal current-velocity relation of skyrmion motion in chiral magnets, Nat. Commun. **4**, 1463 (2013).

[10] S.-Z. Lin, C. Reichhardt, C. D. Batista, and A. Saxena, Driven Skyrmions and Dynamical Transitions in Chiral Magnets, Phys. Rev. Lett. **110**, 207202 (2013).

[11] D. Okuyama, M. Bleuel, J. S. White, Q. Ye, J. Krzywon, G. Nagy, Z. Q. Im, I Zivkovic, M. Bartkowiak, H. M. Rønnow, S. Hoshino, J. Iwasaki, N. Nagaosa, A. Kikkawa, Y. Taguchi, Y. Tokura, D. Higashi, J. D. Reim, Y. Nambu, and T. J. Sato, Deformation of the moving magnetic skyrmion lattice in MnSi under electric current flow, Commun. Phys. **2**, 79 (2019).

[12] D. Liang, J. P. DeGrave, M. J. Stolt, Y. Tokura, and S. Jin, Current-driven dynamics of skyrmions stabilized in MnSi nanowires revealed by topological Hall effect, Nat. Commun. **6**, 8217 (2015).

[13] C. Reichhardt, D. Ray, and C. J. Olson Reichhardt, Collective Transport Properties of Driven Skyrmions with Random Disorder, Phys. Rev. Lett. **114**, 217202 (2015).

[14] W. Jiang, X. Zhang, G. Yu, W. Zhang, X. Wang, M. B. Jungfleisch, J. E. Pearson, X. Cheng, O. Heinonen, K. L. Wang, Y. Zhou, A. Hoffmann, and S. G. E. te Velthuis, Direct observation of the skyrmion Hall effect, Nat. Phys. **13**, 162 (2017).

[15] W. Legrand, D. Maccariello, N. Reyren, K. Garcia, C. Moutafis, C. Moreau-Luchaire, S. Coffin, K. Bouzehouane, V. Cros, and A. Fert, Room-temperature current-induced generation and motion of sub-100 nm skyrmions, Nano Lett. **17**, 2703 (2017).

[16] T. Sato, W. Koshibae, A. Kikkawa, T. Yokouchi, H. Oike, Y. Taguchi, N. Nagaosa, Y. Tokura, and F. Kagawa, Slow steady flow of a skyrmion lattice in a confined geometry probed by narrow-band resistance noise, Phys. Rev. B **100**, 094410 (2019).

[17] S. A. Díaz, C. J. O. Reichhardt, D. P. Arovas, A. Saxena, and C. Reichhardt, Fluctuations and noise signatures of driven magnetic skyrmions, Phys. Rev. B **96**, 085106 (2017).

[18] C. Reichhardt and C. J. Olson Reichhardt, Depinning and nonequilibrium dynamic phases of particle assemblies driven over random and ordered substrates: A review, Rep. Prog. Phys. **80**, 026501 (2017).

[19] K. Everschor-Sitte, J. Masell, R. M. Reeve, and M. Kläui, Perspective: Magnetic skyrmions - Overview of recent progress in an active research field, J. Appl. Phys. **124**, 240901 (2018).

[20] J. Zang, M. Mostovoy, J. H. Han, and N. Nagaosa, Dynamics of Skyrmion Crystals in Metallic Thin Films, Phys. Rev. Lett. **107**, 136804 (2011).

[21] K. Everschor-Sitte and M. Sitte, Real-space Berry phases: Skyrmion soccer (invited), J. Appl. Phys. **115**, 172602 (2014).

[22] B. S. Kim, Skyrmions and Hall transport, J. Phys.: Condens. Matter **31**, 383001 (2019).

[23] Y.-H. Liu and Y.-Q. Li, A mechanism to pin skyrmions in chiral magnets, J. Phys.: Condens. Matter **25**, 076005 (2013).

[24] J. Müller and A. Rosch, Capturing of a magnetic skyrmion with a hole, Phys. Rev. B **91**, 054410 (2015).

[25] F. Büttner, C. Moutafis, M. Schneider, B. Krüger, C. M. Günther, J. Geilhufe, C. von Kor Schmising, J. Mohanty, B. Pfau, S. Schaffert, A. Bisig, M. Foerster, T. Schulz, C. A. F. Vaz, J. H. Franken, H. J. M. Swagten, M. Kläui, and S. Eisebitt, Dynamics and inertia of skyrmionic spin structures, Nat. Phys. **11**, 225 (2015).

[26] C. Reichhardt and C. J. Olson Reichhardt, Noise fluctuations and drive dependence of the skyrmion Hall effect in disordered systems, New J. Phys. **18**, 095005 (2016).

[27] J.-V. Kim and M.-W. Yoo, Current-driven skyrmion dynamics in disordered films, Appl. Phys. Lett. **110**, 132404 (2017).

[28] K. Litzius, I. Lemesh, B. Krüger, P. Bassirian, L. Caretta, K. Richter, F. Büttner, K. Sato, O. A. Tretiakov, J. Förster, R. M. Reeve, M. Weigand, L. Bykova, H. Stoll, G. Schütz, G. S. D. Beach, and M. Kläui, Skyrmion Hall effect revealed by direct time-resolved X-ray microscopy, Nat. Phys. **13**, 170 (2017).

[29] S. Woo, K. M. Song, X. Zhang, Y. Zhou, M. Ezawa, X. Liu, S. Finizio, J. Raabe, N. J. Lee, S. Kim, S.-Y. Park, Y. Kim, J.-Y. Kim, D. Lee, O. Lee, J. W. Choi, B.-C. Min, H. C. Koo, and J. Chang, Current-driven dynamics and inhibition of the skyrmion Hall effect of ferrimagnetic skyrmions in GdFeCo films, Nat. Commun. **9**, 959 (2018).

[30] R. Juge, S.-G. Je, D. de Souza Chaves, L. D. Buda-Prejbeanu, J. Peña-Garcia, J. Nath, I. M. Miron, K. G. Rana, L. Aballe, M. Foerster, F. Genuzio, T. O. Menteş, A. Locatelli, F. Maccherozzi, S. S. Dhesi, M. Belmeguenai, Y. Roussigné, S. Auffret, S. Pizzini, G. Gaudin, J. Vogel, and O. Boulle, Current-Driven Skyrmion Dynamics and Drive-Dependent Skyrmion Hall Effect in an Ultrathin Film, Phys. Rev. Applied **12**, 044007 (2019).

[31] K. Zeissler, S. Finizio, C. Barton, A. Huxtable, J. Massey, J. Raabe, A. V. Sadovnikov, S. A. Nikitov, R. Brearton, T. Hesjedal, G. van der Laan, M. C. Rosamond, E. H. Linfield, G. Burnell, and C. H. Marrows, Diameter-independent skyrmion Hall angle in the plastic flow regime observed in chiral magnetic multilayers, Nature Commun. **11**, 428 (2020).

[32] C. Reichhardt and C. J. O. Reichhardt, Thermal creep and the skyrmion Hall angle in driven skyrmion crystals, J. Phys.: Condens. Matter **31**, 07LT01 (2019).

[33] B. L. Brown, C. Reichhardt, and C. J. O. Reichhardt, Reversible to irreversible transitions in periodically driven skyrmion systems, New J. Phys. **21**, 013001 (2019).

[34] W. Koshibae and N. Nagaosa, Theory of current-driven skyrmions in disordered magnets, Sci. Rep. **8**, 6328 (2018).

[35] S. A. Montoya, R. Tolley, I. Gilbert, S.-G. Je, M.-Y. Im, and E. E. Fullerton, Spin-orbit torque induced dipole skyrmion motion at room temperature, Phys. Rev. B **98**, 104432 (2018).

[36] S. A. Díaz, C. Reichhardt, D. P. Arovas, A. Saxena, and C. J. O. Reichhardt, Avalanches and Criticality in Driven Magnetic Skyrmions, Phys. Rev. Lett. **120**, 117203 (2018).

[37] A. Singh, J. C. T. Lee, K. E. Avila, Y. Chen, S. A. Montoya, E. E. Fullerton, P. Fischer, K. A. Dahmen, S. D. Kevan, M. K. Sanyal, and S. Roy, Scaling of domain cascades in stripe and skyrmion phases, Nat. Commun. **10**, 1988 (2019).

[38] S. Bhattacharya and M. J. Higgins, Dynamics of a Disordered Flux Line Lattice, Phys. Rev. Lett. **70**, 2617 (1993).

[39] C. J. Olson, C. Reichhardt, and F. Nori, Nonequilibrium Dynamic Phase Diagram for Vortex Lattices, Phys. Rev. Lett. **81**, 3757 (1998).

[40] T. Bohlein, J. Mikhael, and C. Bechinger, Observation of kinks and antikinks in colloidal monolayers driven across ordered surfaces, Nat. Mater. **11**, 126 (2012).

[41] P. Tierno, Depinning and Collective Dynamics of Magnetically Driven Colloidal Monolayers, Phys. Rev. Lett. **109**, 198304 (2012).

[42] C. Reichhardt, C. J. Olson, N. Grønbech-Jensen, and F. Nori, Moving Wigner Glasses and Smectics: Dynamics of Disordered Wigner Crystals, Phys. Rev. Lett. **86**, 4354 (2001).

[43] P. Brussarski, S. Li, S. V. Kravchenko, A. A. Shashkin, and M. P. Sarachik, Transport evidence for a sliding two-dimensional quantum electron solid, Nat. Commun. **9**, 3803 (2018).

[44] G. Grüner, The dynamics of charge-density waves, Rev. Mod. Phys. **60**, 1129 (1988).

[45] R. Seshadri and R. M. Westervelt, Forced Shear Flow of Magnetic Bubble Arrays, Phys. Rev. Lett. **70**, 234 (1993).

[46] R. Seshadri and R. M. Westervelt, Collective transport and shear flow of magnetic bubble arrays, Phys. Rev. B **47**, 8620 (1993).

[47] K. H. Nagamanasa, S. Gokhale, A. K. Sood, and R. Ganapathy, Direct measurements of growing amorphous order and non-monotonic dynamic correlations in a colloidal glass-former, Nat. Phys. **11**, 403 (2015).

[48] M. C. Marchetti and D. R. Nelson, Hydrodynamics of flux liquids, Phys. Rev. B **42**, 9938 (1990).

[49] M. C. Marchetti and D. R. Nelson, Patterned geometries and hydrodynamics at the vortex Bose glass transition, Phys. Rev. B **59**, 13624 (1999).

[50] M. Basset, G. Jakob, G. Wirth, and H. Adrian, Patterned irradiation of YBa$_2$Cu$_3$O$_{7-x}$ thin films, Phys. Rev. B **64**, 024525 (2001).

[51] W. K. Kwok, R. J. Olsson, G. Karapetrov, U. Welp, V. Vlasko-Vlasov, K. Kadowaki, and G. W. Crabtree, Modification of vortex behavior through heavy ion lithography, Physica C **382**, 137 (2002).

[52] S. S. Banerjee, A. Soibel, Y. Myasoedov, M. Rappaport, E. Zeldov, M. Menghini, Y. Fasano, F. de la Cruz, C. J. van der Beek, M. Konczykowski, and T. Tamegai, Melting of "porous" Vortex Matter, Phys. Rev. Lett. **90**, 087004 (2003).

[53] R. Besseling, P. H. Kes, T. Drose, and V. M. Vinokur, Depinning and dynamics of vortices confined in mesoscopic flow channels, New J. Phys. **7**, 71 (2005).

[54] Y. Togawa, K. Harada, T. Akashi, H. Kasai, T. Matsuda, F. Nori, A. Maeda, and A. Tonomura, Direct Observation of Rectified Motion of Vortices in a Niobium Superconductor, Phys. Rev. Lett. **95**, 087002 (2005).

[55] K. Yu, T. W. Heitmann, C. Song, M. P. DeFeo, B. L. T. Plourde, M. B. S. Hesselberth, and P. H. Kes, Asymmetric weak-pinning superconducting channels: Vortex ratchets, Phys. Rev. B **76**, 220507(R) (2007).

[56] O. V. Dobrovolskiy, E. Begun, M. Huth, and V. A. Shklovskij, Electrical transport and pinning properties of Nb thin films patterned with focused ion beam-milled washboard nanostructures, New J. Phys. **14**, 113027 (2012).

[57] C. Reichhardt and C. J. Olson Reichhardt, Commensurability effects at nonmatching fields for vortices in diluted periodic pinning arrays, Phys. Rev. B **76**, 094512 (2007).

[58] M. Kemmler, D. Bothner, K. Ilin, M. Siegel, R. Kleiner, and D. Koelle, Suppression of dissipation in Nb thin films with triangular antidot arrays by random removal of pinning sites, Phys. Rev. B **79**, 184509 (2009).

[59] G. J. Kimmel, A. Glatz, V. M. Vinokur, and I. A. Sadovskyy, Edge effect pinning in mesoscopic superconducting strips with non-uniform distribution of defects, Sci. Rep. **9**, 211 (2019).

[60] D. Ray, C. Reichhardt, and C. J. Olson Reichhardt, Pinning, ordering, and dynamics of vortices in conformal crystal and gradient pinning arrays, Phys. Rev. B **90**, 094502 (2014).

[61] Y. L. Wang, M. L. Latimer, Z. L. Xiao, R. Divan, L. E. Ocola, G. W. Crabtree, and W. K. Kwok, Enhancing the critical current of a superconducting film in a wide range of magnetic fields with a conformal array of nanoscale holes, Phys. Rev. B **87**, 220501(R) (2013).

[62] S. Guénon, Y. J. Rosen, A. C. Basaran, and I. K. Schuller, Highly effective superconducting vortex pinning in conformal crystals, Appl. Phys. Lett. **102**, 252602 (2013).

[63] M. Motta, F. Colauto, W. A. Ortiz, J. Fritzsche, J. Cuppens, W. Gillijns, V. V. Moshchalkov, T. H. Johansen, A. Sanchez, and A. V. Silhanek, Enhanced pinning in superconducting thin films with graded pinning landscapes, Appl. Phys. Lett. **102**, 212601 (2013).

[64] C. Reichhardt and C. J. O. Reichhardt, Vortex shear banding transitions in superconductors with inhomogeneous pinning arrays, J. Phys. Commun. **3**, 125009 (2019).

[65] X. B. Xu, H. Fangohr, S. Y. Ding, M. Gu, T. B. Tang, Z. H. Han, D. Q. Shi, and S. X. Dou, Apparent negative mobility of vortex matter due to inhomogeneous pinning, Phys. Rev. B **75**, 224507 (2007).

[66] W. Gillijns, A. V. Silhanek, V. V. Moshchalkov, C. J. Olson Reichhardt, and C. Reichhardt, Origin of Reversed Vortex Ratchet Motion, Phys. Rev. Lett. **99**, 247002 (2007).

[67] T. C. Wu, R. Cao, T. J. Yang, L. Horng, J. C. Wu, and J. Koláček, Rectified vortex motion in an Nb film with a spacing-graded array of holes, Solid State Commun. **150**, 280 (2010).

[68] A. F. Isakovic, P. G. Evans, J. Kmetko, K. Cicak, Z. Cai, B. Lai, and R. E. Thorne, Shear Modulus and Plasticity of a Driven Charge Density Wave, Phys. Rev. Lett. **96**, 046401 (2006).

[69] D. López, W. K. Kwok, H. Safar, R. J. Olsson, A. M. Petrean, L. Paulius, and G. W. Crabtree, Spatially Resolved Dynamic Correlation in the Vortex State of High Temperature Superconductors, Phys. Rev. Lett. **82**, 1277 (1999).

[70] M. C. Miguel and S. Zapperi, Tearing transition and plastic flow in superconducting thin films, Nat. Mater. **2**, 477 (2003).

[71] A. Furukawa and Y. Nisikawa, Banding of angular velocity in the current-driven vortex lattice of a type-II superconductor, Phys. Rev. B **73**, 064511 (2006).

[72] N. S. Lin, V. R. Misko, and F. M. Peeters, Dynamics of multishell vortex structures in mesoscopic superconducting Corbino disks, Phys. Rev. B **81**, 134504 (2010).

[73] M.-C. Miguel, A. Mughal, and S. Zapperi, Laminar Flow of a Sheared Vortex Crystal: Scars in Flat Geometry, Phys. Rev. Lett. **106**, 245501 (2011).

[74] Y. J. Rosen, S. Guénon, and I. K. Schuller, Shearing transition in a superconducting vortex lattice subject to periodic pinning, Phys. Rev. B **88**, 174511 (2013).

[75] Y. Kawamura, Y. Matsumura, Y. Yamazaki, S. Kaneko, N. Kokubo, and S. Okuma, Unusual current-voltage characteristics and dynamic correlation of rotating vortex-lattice rings, Supercond. Sci. Technol. **28**, 045002 (2015).

[76] M. Mochizuki, X. Z. Yu, S. Seki, N. Kanazawa, W. Koshibae, J. Zang, M. Mostovoy, Y. Tokura, and N. Nagaosa, Thermally driven ratchet motion of a skyrmion microcrystal and topological magnon Hall effect, Nat. Mater. **13**, 241 (2014).

[77] S. Pöllath, J. Wild, L. Heinen, T. N. G. Meier, M. Kronseder, L. Tutsch, A. Bauer, H. Berger, C. Pfleiderer, J. Zweck, A. Rosch, and C. H. Back, Dynamical Defects in Rotating

Magnetic Skyrmion Lattices, Phys. Rev. Lett. **118**, 207205 (2017).

[78] S. L. Zhang, W. W. Wang, D. M. Burn, H. Peng, H. Berger, A. Bauer, C. Pfleiderer, G. van der Laan, and T. Hesjedal, Manipulation of skyrmion motion by magnetic field gradients, Nat. Commun. **9**, 2115 (2018).

[79] C. P. Bean, Magnetization of high-field superconductors, Rev. Mod. Phys. **36**, 31 (1964).

[80] C. Reichhardt, C. J. Olson, J. Groth, S. Field, and F. Nori, Microscopic derivation of magnetic flux density profiles, magnetization hysteresis loops, and critical currents in strongly pinned superconductors, Phys. Rev. B **52**, 10441 (1995).

[81] C. Reichhardt and C. J. O. Reichhardt, Reentrant pinning, dynamic row reduction, and skyrmion accumulation for driven skyrmions in inhomogeneous pinning arrays, EPL (to be published), arXiv:1908.5999.

[82] M. Han, J. Yan, S. Granick, and E. Luijten, Effective temperature concept evaluated in an active colloid mixture, Proc. Natl. Acad. Sci. (USA) **114**, 7513 (2017).

[83] J. Loehr, D. de las Heras, A. Jarosz, M. Urbaniak, F. Stobiecki, A. Tomita, R. Huhnstock, I. Koch, A. Ehresmann, D. Holzinger, and T. M. Fischer, Colloidal topological insulators, Commun. Phys. **1**, 4 (2018).

[84] S. I. Denisov, T. V. Lyutyy, V. V. Reva, and A. S. Yermolenko, Temperature effects on drift of suspended single-domain particles induced by the Magnus force, Phys. Rev. E **97**, 032608 (2018).

[85] H. Massana-Cid, E. Navarro-Argemí, D. Levis, I. Pagonabarraga, and P. Tierno, Leap-frog transport of magnetically driven anisotropic colloidal rotors, J. Chem. Phys. **150**, 164901 (2019).

[86] G. Wlazłowski, K. Sekizawa, P. Magierski, A. Bulgac, and M. McNeil Forbes, Vortex Pinning and Dynamics in the Neutron Star Crust, Phys. Rev. Lett. **117**, 232701 (2016).

[87] A. Griffin, S. Nazarenko, V. Shukla, and M.-E. Brachet, The vortex-particle Magnus effect, arXiv:1909.11010.

[88] B. C. van Zuiden, J. Paulose, W. T. M. Irvine, D. Bartolo, and V. Vitelli, Spatiotemporal order and emergent edge currents in active spinner materials, Proc. Natl. Acad. Sci. (USA) **113**, 12919 (2016).

[89] C. Reichhardt and C. J. O. Reichhardt, Reversibility, pattern formation, and edge transport in active chiral and passive disk mixtures, J. Chem. Phys. **150**, 064905 (2019).

[90] C. Reichhardt and C. J. O. Reichhardt, Active microrheology, Hall effect, and jamming in chiral fluids, Phys. Rev. E **100**, 012604 (2019).

[91] S.-Z. Lin, C. Reichhardt, C. D. Batista, and A. Saxena, Particle model for skyrmions in metallic chiral magnets: Dynamics, pinning, and creep, Phys. Rev. B **87**, 214419 (2013).

[92] B. L. Brown, U. C. Täuber, and M. Pleimling, Skyrmion relaxation dynamics in the presence of quenched disorder, Phys. Rev. B **100**, 024410 (2019).

[93] L. Xiong, B. Zheng, M. H. Jin, and N. J. Zhou, Collective transport properties of skyrmions on the depinning phase transition, Phys. Rev. B **100**, 064426 (2019).

[94] C. Reichhardt and C. J. Olson Reichhardt, Magnus-induced dynamics of driven skyrmions on a quasi-one-dimensional periodic substrate, Phys. Rev. B **94**, 094413 (2016).

[95] P. Ao and D. J. Thouless, Berry's Phase and the Magnus Force for a Vortex Line in a Superconductor, Phys. Rev. Lett. **70**, 2158 (1993).

[96] C. Reichhardt and F. Nori, Phase Locking, Devil's Staircases, Farey Trees, and Arnold Tongues in Driven Vortex Lattices with Periodic Pinning, Phys. Rev. Lett. **82**, 414 (1999).

[97] P. T. Korda, M. B. Taylor, and D. G. Grier, Kinetically Locked-in Colloidal Transport in an Array of Optical Tweezers, Phys. Rev. Lett. **89**, 128301 (2002).

[98] C. Reichhardt, D. Ray, and C. J. Olson Reichhardt, Quantized transport for a skyrmion moving on a two-dimensional periodic substrate, Phys. Rev. B **91**, 104426 (2015).

[99] J. Feilhauer, S. Saha, J. Tobik, M. Zelent, L. J. Heyderman, and M. Mruczkiewicz, Controlled motion of skyrmions in a magnetic antidot lattice, arXiv:1910.7388.

[100] C. Reichhardt, D. Ray, and C. J. O. Reichhardt, Nonequilibrium phases and segregation for skyrmions on periodic pinning arrays, Phys. Rev. B **98**, 134418 (2018).

[101] C. Reichhardt and C. J. O. Reichhardt, Nonlinear transport, dynamic ordering, and clustering for driven skyrmions on random pinning, Phys. Rev. B **99**, 104418 (2019).